

<sub>1</sub> Physics-Infused Reduced-Order Modeling for Analysis of  
<sub>2</sub> Ablating Hypersonic Thermal Protection Systems

<sub>3</sub>

<sub>4</sub> November 26, 2025

<sub>5</sub>

## Abstract

This work presents a *physics-infused reduced-order modeling* (PIROM) framework towards design, analysis, and optimization of non-decomposing ablating hypersonic thermal protection systems (TPS), and is demonstrated via the modeling of transient thermo-ablative responses of multi-layered hypersonic TPS. The PIROM architecture integrates a reduced-physics backbone, based on the lumped-capacitance model (LCM) and a surface recession model (SRM), with data-driven correction dynamics formulated via a coarse-graining approach rooted in the Mori-Zwanzig formalism. The LCM is coupled to the SRM to capture the one-dimensional surface recession of the ablating TPS as a function of the surface temperature. While the LCM and SRM capture the dominant physics of the ablating TPS response, the correction terms compensate for residual dynamics arising from higher-order non-linear interactions and temperature-advection effects due to surface recession. The PIROM consistently achieves errors of  $\approx 0.5\%$  for a wide range of extrapolative settings of design parameters involving time-and-space varying boundary conditions and SRM models, and improves by an order of magnitude by the LCM alone. Moreover, the PIROM delivers online evaluations that are two orders of magnitude faster than the full-order model (FOM). These results demonstrate that PIROM effectively reconciles the trade-offs between accuracy, generalizability, and efficiency, providing a promising framework for optimizing multi-physical dynamical systems, such as TPS, under diverse operating conditions.

<sub>25</sub>

## 1 Introduction

<sub>26</sub> At hypersonic speeds, aerospace vehicles experience extreme aero-thermo-dynamic environments that require specialized thermal protection systems (TPS) to shield internal sub-  
<sub>27</sub> structures, electronics, and possibly crew members from the intense aerodynamic heating.  
<sub>28</sub> The TPS is composed of ablating materials to withstand the high-energy physics – a high-  
<sub>29</sub> temperature capable fibrous material injected with a resin that fills the pore network and  
<sub>30</sub> strengthens the composite [1]. The TPS design promotes the exchange of mass through  
<sub>31</sub> thermal and chemical reactions (i.e., ablation), effectively mitigating heat transfer to the  
<sub>32</sub> sub-structures. As a result, accurate prediction for the ablating TPS response under ex-  
<sub>33</sub> treme hypersonic heating becomes critical to ensuring survivability, performance, and safety  
<sub>34</sub> of hypersonic vehicles. Not only is it necessary to assess the performance of the thermal  
<sub>35</sub> environment, but also to ensure the integrity of the vehicle's structure and systems under extreme

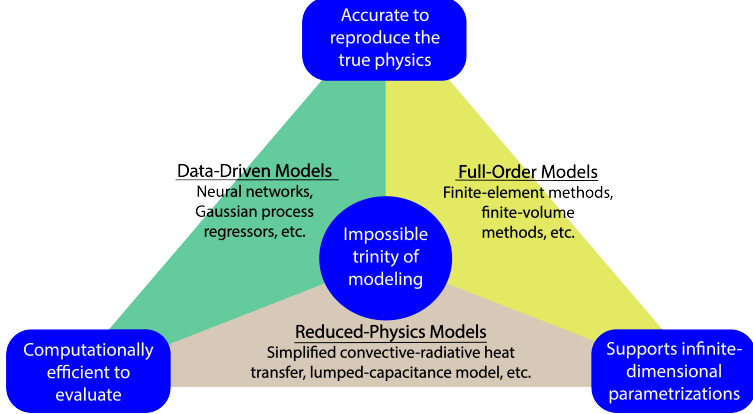


Figure 1: The impossible trinity of modeling: accuracy, generalizability, and efficiency.

management systems, but also the shape changes of the vehicle’s outer surface induced by the ablating material, and its impact on the aerodynamics, structural integrity, and controllability.

Even with today’s advancements in computational resources and numerical methods, high-fidelity simulations of ablating TPS remains a formidable challenge, both theoretically and computationally. On the theoretical side, the thermo-chemical reactions, coupled with the irregular pore network structure and ablating boundaries, translate into complex non-linear equations governing multi-physical interactions across several spatio-temporal scales [1, 8]. On the computational side, numerical approaches based on finite-element (FEM) or finite-volume (FVM) methods yield systems of differential equations modeling the transient thermo-ablative response of the TPS [5]. The FEM discretizations lead to high-dimensional systems of equations, resulting in prohibitive computational costs for many-query applications such as design, optimization, uncertainty quantification, and real-time applications, where possibly thousands of model evaluations are required.

Reduced-order models (ROMs) have emerged as a promising approach to alleviate the computational costs of high-fidelity simulations [6, 11]. Ideally, a ROM should be: (1) accurate to reproduce high-fidelity solutions, (2) support continuous or infinite-dimensional design parameters such as geometrical shapes and material distributions, (3) be computationally efficient to evaluate to allow for fast turnaround times in design optimization. However, the above three capabilities usually form an *impossible trinity of modeling*, as illustrated in Fig. 1; building a ROM that achieves any two capabilities sacrifices the third.

The impossible trinity poses a significant challenge in the development of ROMs for the multi-disciplinary transient analysis and optimization of ablating TPS. Specifically, full-order models (FOMs), e.g., FEMs or FVMs, offer high accuracy and robust generalization over design spaces, but are computationally expensive to evaluate. Reduced-physics models (RPMs) – such as simplified convective-radiative heat transfer or engineering correlations – are low-dimensional models that achieve efficiency and broad applicability by ignoring higher-order non-linear effects. However, RPMs sacrifice accuracy for complex thermo-ablative responses due to the simplifications and assumptions inherent in their formulation, and it is generally not clear how to systematically leverage existing high-fidelity data to improve RPMs [18].

67 Lastly, data-driven ROMs, such as Gaussian Process Regression (GPR) [? ], Neural Net-  
68 works (NNs), and neural ordinary differential equations (NODEs) [3], can provide accurate  
69 and computationally-efficient approximations of high-fidelity models for complex thermo-  
70 ablative responses. However, these data-centric approaches often demand extensive high-  
71 fidelity data for training, do not necessarily satisfy fundamental physical constraints or con-  
72 servation laws, and thus do not generalize well to the design spaces outside the training [16].

73 This work presents the extension of the *physics-infused reduced-order modeling* (PIROM)  
74 framework to include effects of ablation for TPS applications, previously ignored in Ref. [17].  
75 Specifically, the PIROM is demonstrated for the transient thermo-ablative response of multi-  
76 layered hypersonic TPS. The PIROM is a non-intrusive framework that combines the strengths  
77 of physics-based models with machine learning to formulate and train ROMs for parametrized  
78 non-linear dynamical systems. The backbone of the PIROM is the physics-based component,  
79 i.e., the RPM, which in this work is composed of: (1) a *lumped capacitance model* (LCM)  
80 to model the average heat transfer within the TPS layers, and (2) a *surface recession model*  
81 (SRM) to model one-dimensional surface ablation.

82 Leveraging the *Mori-Zwanzig* (MZ) formalism [15, 14, 13], the RPM is rigorously ex-  
83 tended with data-driven hidden dynamics to account for the missing physics in the LCM,  
84 which are learned from high-fidelity data. The hidden dynamics enable higher predictive  
85 accuracy of the PIROM when subjected to complex boundary conditions and SRM model  
86 variations. For the TPS problem, the MZ approach produces a sufficiently simple model  
87 form while maintaining the physical consistency of the PIROM, as well as the dependence  
88 on design parameters. Thus, the PIROM aims to solve the ITM by leveraging the gen-  
89 eralizability and computational efficiency of RPMs, while incorporating the accuracy and  
90 adaptability of data-driven extensions. More importantly, the PIROM formulation provides  
91 a general methodology for developing PIROMs for other multi-physics problems.

92 The specific objectives of this work are summarized as follows:

- 93 1. Extend the previous PIROM formulation in Ref. [17] to model transient thermo-  
94 ablative response of multi-layered hypersonic TPS through a systematic coarse-graining  
95 procedure based on the Mori-Zwanzig formalism.
- 96 2. Benchmark the accuracy, generalizability, and computational accelerations of the PIROM  
97 against the RPM and the high-fidelity FEM solutions of ablating TPS, thus quanti-  
98 fying the PIROM’s capabilities to solve the ITM in complex multi-physical non-linear  
99 dynamical systems.

## 100 2 Modeling of Thermal Protection Systems

101 This section presents the problem of modeling the transient thermo-ablative response of a  
102 non-decomposing TPS, subjected to extreme hypersonic heating. Two different but math-  
103 ematically connected solution strategies are provided: (1) a high-fidelity full-order model  
104 (FOM) based on a finite element method (FEM), and (2) a RPM based on a *lumped ca-*  
105 *pacitance model* (LCM) and a one-dimensional *surface recession model* (SRM). The FOM is  
106 computationally expensive but provides the highest fidelity, while the RPM is computa-  
107 tionally efficient but has low predictive fidelity. However, both models are physically consistent

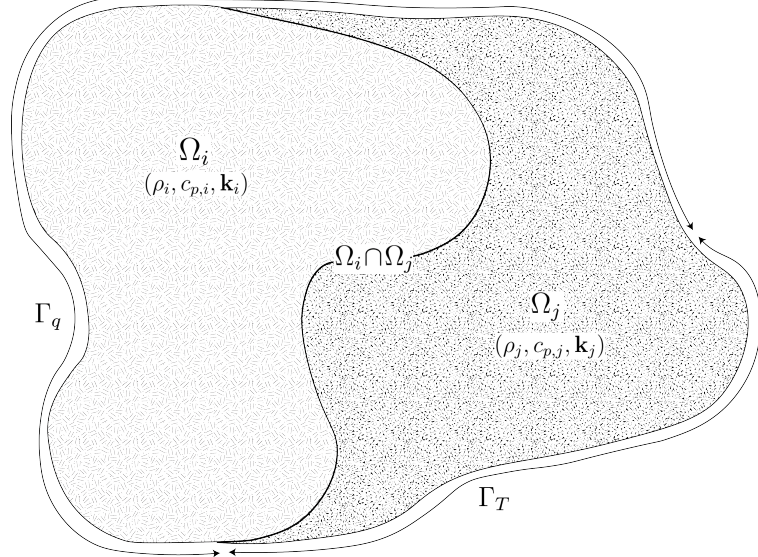


Figure 2: General domain  $\Omega$  with prescribed Neumann and Dirichlet boundary conditions on  $\Gamma_q$  and  $\Gamma_T$ . Mesh displacement  $w(x, t)$  occurs on the  $\Gamma_q$  boundary.

108 to high-dimensional design variables. The following discussion presents the TPS modeling  
109 problem and the FOM and RPM solution strategies.

## 110 2.1 Governing Equations

111 The multi-physics of a non-decomposing ablating TPS under a hypersonic boundary layer  
112 involves the *energy equation* for heat conduction inside the TPS, and the *pseudo-elasticity*  
113 *equation* for mesh motion due to surface recession. The coupling between these two equations  
114 occurs at the heated boundary, where the surface temperature drives the surface recession  
115 velocity, which appears as an advection term in the energy equation. The governing PDEs  
116 are described as follows.

### 117 2.1.1 Energy Equation

118 Consider a generic domain  $\Omega \subset \mathbb{R}^d$ ,  $d = 2$  or  $3$ , illustrated in Fig. 2. Let  $\partial\Omega = \Gamma_q \cup \Gamma_T$   
119 and  $\Gamma_q \cap \Gamma_T = \emptyset$ , where a Neumann  $q_b(x, t)$  boundary condition is prescribed on the heated  
120 boundary  $\Gamma_q$ , and represents the surface exposed to the hypersonic boundary layer. The  
121 Dirichlet  $T_b(x, t)$  boundary condition is prescribed on the boundary  $\Gamma_T$ . The TPS is divided  
122 into  $N$  non-overlapping components  $\{\Omega_i\}_{i=1}^N$ , as illustrated in Fig. 2 for  $N = 2$ . The  $i$ -th  
123 component  $\Omega_i$  is associated with material properties  $(\rho_i, c_{p,i}, \mathbf{k}_i)$ , which are continuous within  
124 one component, and can be discontinuous across two neighboring components.

125 The energy equation describes the transient heat conduction,

$$\rho c_p \left( \frac{\partial T}{\partial t} + \tilde{\mathbf{v}}(x, t) \cdot \nabla T \right) - \nabla \cdot (\mathbf{k} \nabla T) = 0, \quad x \in \Omega \quad (1a)$$

$$-\mathbf{k} \nabla T \cdot \mathbf{n} = q_b(x, t), \quad x \in \Gamma_q \quad (1b)$$

$$T(x, t) = T_b(x, t), \quad x \in \Gamma_T \quad (1c)$$

$$T(x, 0) = T_0(x), \quad x \in \Omega \quad (1d)$$

126 where  $\rho$ ,  $c_p$ , and  $\mathbf{k} \in \mathbb{R}^{d \times d}$  are the constant density, heat capacity, and thermal conductivity.  
127 Note that our prior work has applied the PIROM to TPS problems with temperature-varying  
128 material properties [17]. In the order they appear, the  $\rho c_p \frac{\partial T}{\partial t}$  term includes the unsteady  
129 energy storage,  $\rho c_p \tilde{\mathbf{v}}(x, t) \cdot \nabla T$  includes the temperature advection due to ablation, and  
130  $\nabla \cdot (\mathbf{k} \nabla T)$  includes the heat conduction. The boundary conditions for the energy equation  
131 include Neumann eq. (1b) on  $\Gamma_q$  and Dirichlet eq. (1c) on  $\Gamma_T$ , and the initial condition is  
132 provided in eq. (1d).

133 An Arbitrary Lagrangian-Eulerian (ALE) description is used to account for mesh motion  
134 due to surface recession. The relative velocity of the material  $\tilde{\mathbf{v}}(x, t)$  with respect to the  
135 mesh is,

$$\tilde{\mathbf{v}}(x, t) = \mathbf{v}_s(x, t) - \mathbf{v}_m(x, t) \quad (2)$$

136 where  $\mathbf{v}_s(x, t)$  and  $\mathbf{v}_m(x, t)$  are the physical material velocity and mesh velocity, respectively.  
137 In this work, the physical material velocity is assumed to be zero, i.e.,  $\mathbf{v}_s(x, t) = \mathbf{0}$ , and thus  
138 the relative velocity is simply the negative of the mesh velocity,  $\tilde{\mathbf{v}}(x, t) = -\mathbf{v}_m(x, t)$ .

### 139 2.1.2 Pseudo-Elasticity Equation

140 The mesh displacements  $\mathbf{d} \in \mathbb{R}^d$  are described by the steady-state pseudo-elasticity equation,  
141 which models the mesh as a fictitious elastic solid that deforms according to the prescribed  
142 boundary displacements. The governing equation is given as,

$$\nabla \cdot \boldsymbol{\sigma}(\mathbf{d}) = \mathbf{0}, \quad \forall t \in \mathcal{T}, \quad x \in \Omega \quad (3a)$$

$$\mathbf{d}(x, t) = \mathbf{d}_q(x, t), \quad \forall t \in \mathcal{T}, \quad x \in \Gamma_q \quad (3b)$$

$$\mathbf{d}(x, t) = \mathbf{0}, \quad \forall t \in \mathcal{T}, \quad x \in \Gamma_T \quad (3c)$$

$$\mathbf{d}(x, 0) = \mathbf{0}, \quad \forall x \in \Omega \quad (3d)$$

143 where the stress tensor  $\boldsymbol{\sigma}$  is related to the strain tensor  $\boldsymbol{\epsilon}(\mathbf{d})$  through Hooke's law,

$$\boldsymbol{\sigma}(\mathbf{d}) = \mathbb{D} : \boldsymbol{\epsilon}(\mathbf{d})$$

144 where  $\mathbb{D}$  is the fourth-order positive definite elasticity tensor, and “ $:$ ” is the double con-  
145 traction of the full-order tensor  $\mathbb{D}$  with the second-order tensor  $\boldsymbol{\epsilon}$ . The elasticity tensor  
146 ordinarily possess a number of symmetries, effectively reducing the number of components  
147 that describe it [2]. The symmetric strain tensor  $\boldsymbol{\epsilon}$  measures the deformation of the mesh

<sup>148</sup> due to displacements  $\mathbf{d}(x, t)$ , and is defined as,

$$\boldsymbol{\epsilon}(\mathbf{d}) = \frac{1}{2} (\nabla \mathbf{d} + \nabla \mathbf{d}^\top)$$

<sup>149</sup> The “material” properties for the mesh are chosen to tailor the mesh deformation, and need  
<sup>150</sup> not represent the actual material being modeled [1].

<sup>151</sup> For the pseudo-elasticity equations, the boundary conditions include prescribed displace-  
<sup>152</sup> ments  $\mathbf{d}_q(x, t)$  on the heated boundary  $\Gamma_q$  in eq. (3b), and zero displacements on the unheated  
<sup>153</sup> boundaries in eq. (3c). The initial condition for the mesh displacements is zero in eq. (3d).  
<sup>154</sup> Particularly, the surface velocity due to the ablating material is a function of the surface  
<sup>155</sup> temperature  $T_q(x, t)$  for  $x \in \Gamma_q$  on the heated boundary. For the  $i$ -th material component,  
<sup>156</sup> the mesh velocity on the heated boundary is imposed based on the following relation,

$$\hat{\mathbf{n}} \cdot \mathbf{v}_m(x, t) = f_i(T_q(x, t)), \quad x \in \Gamma_q \quad (4)$$

<sup>157</sup> where  $\hat{\mathbf{n}}$  is the unit normal vector on the heated boundary  $\Gamma_q$ , and  $f_i$  is a material-dependent  
<sup>158</sup> function obtained from tabulated data, commonly referred to as a B’ table [1]. The B’ table  
<sup>159</sup> provides a model for the recession velocity as a function of the surface temperature, and is pre-  
<sup>160</sup> computed based on high-fidelity simulations or physical experiments for a one-dimensional  
<sup>161</sup> slab of materials, and is independent of the TPS geometry. Provided the surface velocity,  
<sup>162</sup> the boundary condition in eq. (5) for the mesh displacements are computed by integrating  
<sup>163</sup> the surface velocity over time,

$$\mathbf{d}_q(x, t) = \int_0^t \mathbf{v}_m(x, \tau) d\tau \quad (5)$$

## <sup>164</sup> 2.2 Full-Order Model: Finite-Element Method

<sup>165</sup> The following discussion presents the FOM for predicting the transient thermo-ablative re-  
<sup>166</sup> sponse of the TPS, based on a finite-element discretization of the governing equations in  
<sup>167</sup> eq. (1), including the energy equation and pseudo-elasticity equation.

<sup>168</sup> **Energy Equation** To obtain the full-order numerical solution, the *energy equation* is spa-  
<sup>169</sup> tially discretized using variational principles of the Discontinuous Galerkin (DG) method [5].  
<sup>170</sup> Note that the choice of DG approach is mainly for theoretical convenience, and is exclusively  
<sup>171</sup> performed on the energy equation, as it is the surface temperature that drives the ablation  
<sup>172</sup> process; the equivalence between DG and FEM is noted upon their convergence. Consider  
<sup>173</sup> a conforming mesh partition domain, where each element belongs to one and only one com-  
<sup>174</sup> ponent. Denote the collection of all  $M$  elements as  $\{E_i\}_{i=1}^M$ . In an element  $E_i$ , its shared  
<sup>175</sup> boundaries with another element  $E_j$ , Neumann BC, and Dirichlet BC are denoted as  $e_{ij}$ ,  $e_{iq}$ ,  
<sup>176</sup> and  $e_{iT}$ , respectively. Lastly,  $|e|$  denotes the length ( $n_d = 2$ ) or area ( $n_d = 3$ ) of a component  
<sup>177</sup> boundary  $e$ . For the  $i$ -th element, use a set of  $P$  trial functions, such as polynomials, to

178 represent the temperature distribution,

$$T_i(x, t) = \sum_{l=1}^P \phi_l^i(x) u_l^i(t) \equiv \boldsymbol{\phi}_i^\top(x) \mathbf{u}(t), \quad i = 1, 2, \dots, M \quad (6)$$

179 Then, the energy equation is collected into a block-system of ODEs for all the elements in  
180 the mesh,

$$\mathbf{A}\dot{\mathbf{u}} = [\mathbf{B} + \mathbf{C}(\mathbf{u})] \mathbf{u} + \mathbf{f}(t) \quad (7)$$

181 where  $\mathbf{u} = [\mathbf{u}_1, \mathbf{u}_2, \dots, \mathbf{u}_M]^\top \in \mathbb{R}^{MP}$  includes all the DG variables,  $\mathbf{f} \in \mathbb{R}^{MP}$  is the external  
182 forcing, and the system matrices  $\mathbf{A}$ ,  $\mathbf{B}$ , and  $\mathbf{C}$  are the matrices due to heat capacity, heat  
183 conduction, and temperature advection due to mesh motion, respectively. Note that the  
184 advection matrix  $\mathbf{C}(\mathbf{u})$  is a function of the temperature  $\mathbf{u}$  since it depends on the mesh  
185 velocity as in eq. (4); this is the main source of non-linearity in the current TPS problem.  
186 A detailed derivation of eq. (7) and their matrices is provided in Appendix A.

187 **Pseudo-Elasticity Equation** The *pseudo-elasticity equation* is spatially discretized using  
188 the standard Galerkin FEM method as implemented in the SIERRA mechanics module on a  
189 structured mesh with quadrilateral elements [2]. Define the scalar basis functions  $\{\psi_q(x)\}_{q=1}^Q$   
190 nodal variables  $\{\mathbf{d}_q\}_{q=1}^Q$  for the mesh displacements, where  $Q$  is the number of basis functions.  
191 Express the mesh displacements  $\mathbf{w}$  at time  $t$  as,

$$\mathbf{w}(x, t) \approx \sum_{q=1}^Q \psi_q(x) \mathbf{w}_q \quad (8)$$

192 Substituting into the Galerkin weak form of the *steady* pseudo-elasticity equation, the fol-  
193 lowing linear system of equations is obtained for the nodal displacements,

$$\mathbf{K}\mathbf{w} = \mathbf{g} \quad (9)$$

194 where  $\mathbf{w}$  is the global displacement vector,  $\mathbf{K} \in \mathbb{R}^{dQ \times dQ}$  the global stiffness matrix of dimen-  
195 sion  $d$ , defined by the volume integrals over the domain  $\Omega$  provided the elasticity tensor  $\mathbb{D}$ ,  
196 and  $\mathbf{g}$  is the global force vector due to the Dirichlet boundary conditions on the heated  $\Gamma_q$   
197 and unheated  $\Gamma_T$  boundaries.

### 198 2.3 Reduced-Physics Model

199 The RPM for predicting the response of the ablating TPS consists of two components: (1)  
200 *surface recession model* (SRM) and a *lumped capacitance model* (LCM). The SRM provides  
201 a relation between the surface temperature and *one-dimensional* surface recession veloc-  
202 ity based on pre-computed B' tables for the material, enabling the computation of *one-*  
203 *dimensional* surface displacements. Provided the geometry changed induced by the surface  
204 recession, the LCM predicts the average temperature inside each component of the TPS,  
205 which are in turn used as low-fidelity estimates for the surface temperatures required by the  
206 SRM. Therefore, the SRM and LCM are coupled to define the RPM, providing low-fidelity

207 estimates for temperatures and surface recessions of the ablating TPS.

### 208 2.3.1 Surface Recession Model

209 The mesh displacements  $\mathbf{d}$  are constrained to be *one-dimensional* on the heated boundary  
210  $\Gamma_q$ , i.e.,  $w_i(x, t) = \mathbf{d}(x, t) \cdot \hat{\mathbf{n}}$ , where  $\hat{\mathbf{n}}$  is the unit normal vector on the heated boundary  
211  $\Gamma_q$ . Displacements perpendicular to  $\hat{\mathbf{n}}$  are assumed small and are neglected. Let  $\mathbf{w} =$   
212  $[w_1, w_2, \dots, w_{\tilde{N}}]^\top \in \mathbb{R}^{\tilde{N}}$  include the displacements for the  $\tilde{N}$  ablating components on the  
213 heated boundary, where  $\tilde{N} \leq N$ . Then the SRM capturing the one-dimensional surface  
214 recession for ablating materials is,

$$\dot{\mathbf{w}} = \boldsymbol{\Xi}\mathbf{u} - \tilde{\mathbf{f}} \quad (10)$$

215 where  $\boldsymbol{\Xi} = \text{diag}(\alpha_1, \dots, \alpha_{\tilde{N}})$  and  $\tilde{\mathbf{f}} = (\alpha_1 u_{0,1}, \dots, \alpha_{\tilde{N}} u_{0,\tilde{N}})^\top$ . The constants  $\alpha_i$  are small  
216 material-dependent constants, determined from the B' table, and  $u_{0,i}$  is the constant initial  
217 temperature of the ablative component. The SRM provides a relation between the surface's  
218 temperature and recession velocity, based on pre-computed B' tables for the material.

### 219 2.3.2 Lumped Capacitance Model

220 A general form of the LCM is provided in this section; details regarding the derivation for  
221 the four-component TPS used in the results section are provided in Appendix A. Let  $\Omega$  be  
222 partitioned into  $N$  non-overlapping components  $\{\Omega_i\}_{i=1}^N$ , as illustrated in Fig. 2 for  $N = 2$ .  
223 The domain  $\Omega$  is a function of the surface displacements  $\mathbf{w}$  on the heated boundary  $\Gamma_q$ , and  
224 thus the geometry of each component  $\Omega_i$  is time-dependent. The LCM predicts the temporal  
225 variation of average temperatures in multiple interconnected components [9]. From a point  
226 of view of energy conservation, the LCM leads to the following system of first-order ODEs  
227 for the average temperatures in the components,

$$\bar{\mathbf{A}}(\mathbf{w})\dot{\bar{\mathbf{u}}} = \bar{\mathbf{B}}(\mathbf{w})\bar{\mathbf{u}} + \bar{\mathbf{f}}(t) \quad (11)$$

228 Where the states and inputs,

$$\bar{\mathbf{u}} = [\bar{u}_1, \bar{u}_2, \dots, \bar{u}_N]^\top \in \mathbb{R}^N, \quad \bar{\mathbf{f}} = [\bar{f}_1, \bar{f}_2, \dots, \bar{f}_N]^\top \in \mathbb{R}^N \quad (12)$$

229 include the average temperatures  $\bar{\mathbf{u}}$  and spatially-integrated inputs  $\bar{\mathbf{f}}$  for the  $N$  components.  
230 For  $i, j = 1, 2, \dots, N$  the  $(i, j)$ -th elements of the  $\bar{\mathbf{A}} \in \mathbb{R}^{N \times N}$ ,  $\bar{\mathbf{B}} \in \mathbb{R}^{N \times N}$ , and  $\bar{\mathbf{f}} \in \mathbb{R}^N$   
231 matrices are given by,

$$\bar{A}_i = \begin{cases} \int_{\Omega_i} \rho c_p d\Omega_i, & i = j \\ 0, & i \neq j \end{cases}, \quad \bar{B}_{ij} = \begin{cases} \sum_{j \in \mathcal{N}_i \cup \{T_b\}} \bar{B}_{ij}^i, & i = j \\ \bar{B}_{ij}^{(j)}, & i \neq j \end{cases}, \quad (13a)$$

$$\mathbf{f}_i = \begin{cases} |e_{iq}| \bar{q}_i + \frac{|e_{iT}|}{R_i} \bar{T}_i, & i = j \\ 0, & i \neq j \end{cases} \quad (13b)$$

<sup>232</sup> where,

$$\bar{q}_i = \frac{1}{|e_{iq}|} \int_{e_{iq}} q_b de_{iq}, \quad \bar{T}_i = \frac{1}{|e_{iT}|} \int_{e_{iT}} T_b de_{iT}, \quad \bar{B}_{ij}^i = -\frac{|e_{ij}|}{R_{ij}}, \quad \bar{B}_{ij}^j = \frac{|e_{ij}|}{R_{ij}} \quad (14)$$

<sup>233</sup> where  $R_{ij}$  is the equivalent thermal resistance between two neighboring components  $\Omega_i$  and  
<sup>234</sup>  $\Omega_j$ , and  $R_i$  is the thermal resistance between component  $\Omega_i$  and the Dirichlet boundary.  
<sup>235</sup> Note that the heat capacitances and thermal resistances are computed based on the current  
<sup>236</sup> geometry of each component, which is a function of the surface displacements  $\mathbf{w}$  on the  
<sup>237</sup> heated boundary  $\Gamma_q$ .

### <sup>238</sup> 2.3.3 Thermo-Ablative Reduced-Physics Model

<sup>239</sup> The SRM and LCM are combined to define the RPM for predicting the thermo-ablative  
<sup>240</sup> response of the TPS under hypersonic boundary layers. Specifically, the RPM is defined as  
<sup>241</sup> the LCM as in eq. (11), where the *geometry-dependent* matrices  $\tilde{\mathbf{A}}$ ,  $\tilde{\mathbf{B}}$ , and  $\tilde{\mathbf{f}}$  are updated  
<sup>242</sup> at each time step based on the current displacements  $\mathbf{w}$  provided by the SRM. The RPM is  
<sup>243</sup> formally stated as,

$$\tilde{\mathbf{A}}(\mathbf{s})\dot{\mathbf{s}} = \tilde{\mathbf{B}}(\mathbf{s})\mathbf{s} + \tilde{\mathbf{F}}(t) \quad (15a)$$

$$\tilde{\mathbf{z}} = \mathbf{s} \quad (15b)$$

<sup>244</sup> where the state  $\mathbf{s} = [\bar{\mathbf{u}}, \mathbf{w}]^\top \in \mathbb{R}^{N+\tilde{N}}$  includes the *average temperature* and *one-dimensional*  
<sup>245</sup> *surface displacements*, and  $\tilde{N}$  is the number of ablating components with  $\tilde{N} \leq N$ . Moreover,  
<sup>246</sup> the observables are defined as  $\mathbf{z} = [\bar{\mathbf{u}}, \mathbf{w}]^\top \in \mathbb{R}^{N+\tilde{N}}$ . The matrices are given as,

$$\tilde{\mathbf{A}}(\mathbf{s}) = \begin{bmatrix} \bar{\mathbf{A}}(\mathbf{s}) & \mathbf{0} \\ \mathbf{0} & \mathbf{I} \end{bmatrix}, \quad \tilde{\mathbf{B}}(\mathbf{s}) = \begin{bmatrix} \bar{\mathbf{B}}(\mathbf{s}) & \mathbf{0} \\ \boldsymbol{\Xi} & \mathbf{0} \end{bmatrix}, \quad \tilde{\mathbf{F}}(t) = \begin{bmatrix} \bar{\mathbf{f}}(t) \\ -\tilde{\mathbf{f}} \end{bmatrix} \quad (16)$$

<sup>247</sup> In the matrices  $\tilde{\mathbf{A}}$  and  $\tilde{\mathbf{B}}$ , the surface displacements  $\mathbf{w}$  are used to define the dimensions for  
<sup>248</sup> the  $\Omega_i$  component used in eqs. (13) and (14), thus effectively coupling the LCM and SRM.

## <sup>249</sup> 2.4 Summary of Modeling Approaches

<sup>250</sup> The FOM (i.e., FEM) and RPM (i.e., LCM with SRM) are two different but mathematically  
<sup>251</sup> connected solution strategies. Particularly, the LCM in eq. (11) not only resembles the  
<sup>252</sup> functional form of the DG model in eq. (7), but can be viewed as a special case of the latter,  
<sup>253</sup> where the mesh partition is extremely coarse, and the trial and test functions are piece-wise  
<sup>254</sup> constants. This removes all spatial variations within each component, and neglects advection  
<sup>255</sup> effects due to mesh motion.

<sup>256</sup> For example, consider the case where each component  $\Omega_i$  is treated as one single element,  
<sup>257</sup> and each element employs one constant basis function  $\phi_i = 1$ . The DG-FEM model for the  
<sup>258</sup>  $i$ -th component simplifies to the scalar ODE,

$$\mathbf{A}^{(i)} = \bar{A}_i, \quad \mathbf{C}^{(i)} = 0, \quad \mathbf{B}_{ij}^{(i)} = -\sigma|e_{ij}|, \quad \mathbf{B}_{ij}^{(j)} = \sigma|e_{ij}|, \quad \mathbf{f}_i = |e_{iq}|\bar{q}_i + \sigma|e_{iT}|\bar{T}_i \quad (17)$$

259 Clearly, the LCM is a coarse zeroth-order DG model with the inverse of thermal resistance  
260 chosen as the element-wise penalty factors. Or conversely, the DG model is a refined version  
261 of LCM via  $hp$ -adaptation.

262 The FOM and RPM represent two extremes in the modeling fidelity and computational  
263 cost spectrum. On one hand, the FOM is the most accurate but computationally expensive  
264 to evaluate due to the fine mesh discretizations for both the temperature and displacement  
265 fields, leading to possibly millions of state variables. On the other hand, the RPM considers  
266 only the average temperature of the material, from which the displacements are obtained by  
267 integrating the velocity. The coarsened representation of the temperature field significantly  
268 reduces the number of state variables to only a few per component, and thus reducing the  
269 computational cost. However, this sacrifices local temperature information that becomes  
270 critical to properly capture higher-order effects due to mesh motion and thermal gradients  
271 within each component. Thus, neither the FOM nor the RPM is an universal approach for  
272 real-world analysis, design, and optimization tasks for ablating TPS, where thousands of  
273 high-fidelity model evaluations may be necessary. This issue motivates the development of  
274 the PIROM, which can achieve the fidelity of FOM at a computational cost close to the  
275 RPM, while maintaining the generalizability to model parameters.

## 276 **3 Physics-Infused Reduced-Order Modeling**

277 The formulation of PIROM for ablating TPS starts by connecting the FOM, i.e., the DG-  
278 FEM, and the RPM, i.e., the LCM, via a coarse-graining procedure. This procedure pin-  
279 points the missing dynamics in the LCM when compared to DG-FEM. Subsequently, the  
280 Mori-Zwanzig (MZ) formalism is employed to determine the model form for the missing dy-  
281 namics in PIROM. Lastly, the data-driven identification of the missing dynamics in PIROM  
282 is presented.

### 283 **3.1 Deriving the Reduced-Physics Model via Coarse-Graining**

284 The subsequent coarse-graining formulation is performed on the DG-FEM in eq. (7) to  
285 derive the LCM in eq. (11). This process constraints the trial function space of a full-  
286 order DG model to a subset of piece-wise constants, so that the variables  $\mathbf{u}$ , matrices  $\mathbf{A}$ ,  
287  $\mathbf{B}$ , and  $\mathbf{C}$ , and forcing vector  $\mathbf{f}$  are all approximated using a single state associated to the  
288 average temperature. Note that the coarse-graining is exclusively performed on the thermal  
289 dynamics, as it is the surface temperature that drives the one-dimensional recession via  
290 the SRM. Hence, the coarse-graining of the mesh dynamics is not included in the following  
291 procedure.

#### 292 **3.1.1 Coarse-Graining of States**

293 Consider a DG model as in eq. (7) for  $M$  elements and an LCM as in eq. (11) for  $N$  compo-  
294 nents; clearly  $M \gg N$ . Let  $\mathcal{V}_j = \{i | E_i \in \Omega_j\}$  be the indices of the elements belonging to the  
295  $j$ -th component, so  $E_i \in \Omega_j$  for all  $i \in \mathcal{V}_j$ . The number of elements in the  $j$ -th component is

<sup>296</sup>  $|\mathcal{V}_j|$ . The average temperature on  $\Omega_j$  is,

$$\bar{u}_j = \frac{1}{|\Omega_j|} \sum_{i \in \mathcal{V}_j} \int_{E^{(i)}} \boldsymbol{\phi}^{(i)}(x)^T \mathbf{u}^{(i)} d\Omega = \frac{1}{|\Omega_j|} \sum_{i \in \mathcal{V}_j} |E_i| \boldsymbol{\varphi}_i^{j\top} \mathbf{u}^{(i)}, \quad j = 1, 2, \dots, N \quad (18)$$

<sup>297</sup> where  $|\Omega_j|$  and  $|E_i|$  denote the area ( $d = 2$ ) or volume ( $d = 3$ ) of component  $j$  and element <sup>298</sup>  $i$ , respectively. The orthogonal basis functions are defined as  $\boldsymbol{\varphi}_i^{j\top} = [1, 0, \dots, 0]^\top \in \mathbb{R}^P$ .

<sup>299</sup> Conversely, given the average temperatures of the  $N$  components,  $\bar{\mathbf{u}}$ , the states of an <sup>300</sup> arbitrary element  $E_i$  is written as,

$$\mathbf{u}^{(i)} = \sum_{k=1}^N \boldsymbol{\varphi}_i^k \bar{u}_k + \delta \mathbf{u}^{(i)}, \quad i = 1, 2, \dots, M \quad (19)$$

<sup>301</sup> where  $\boldsymbol{\varphi}_i^k = 0$  if  $i \notin \mathcal{V}_k$ , and  $\delta \mathbf{u}^{(i)}$  represents the deviation from the average temperature and <sup>302</sup> satisfies the orthogonality condition  $\boldsymbol{\varphi}_i^{k\top} \delta \mathbf{u}^{(i)} = 0$  for all  $k$ .

<sup>303</sup> Equations eqs. (18) and (19) are combined and written in matrix form as,

$$\bar{\mathbf{u}} = \boldsymbol{\Phi}^+ \mathbf{u}, \quad \mathbf{u} = \boldsymbol{\Phi} \mathbf{u} + \delta \mathbf{u} \quad (20)$$

<sup>304</sup> where  $\boldsymbol{\Phi} \in \mathbb{R}^{MP \times N}$  is a matrix of  $M \times N$  blocks, with the  $(i, j)$ -th block as  $\boldsymbol{\varphi}_i^j$ ,  $\boldsymbol{\Phi}^+ \in \mathbb{R}^{N \times MP}$  <sup>305</sup> is the left inverse of  $\boldsymbol{\Phi}$ , with the  $(i, j)$ -th block as  $\boldsymbol{\varphi}_i^{j+} = \frac{|E_i|}{|\Omega_j|} \boldsymbol{\varphi}_i^{j\top}$ , and  $\delta \mathbf{u}$  is the collection of <sup>306</sup> deviations. By their definitions,  $\boldsymbol{\Phi}^+ \boldsymbol{\Phi} = \mathbf{I}$  and  $\boldsymbol{\Phi}^+ \delta \mathbf{u} = \mathbf{0}$ .

### <sup>307</sup> 3.1.2 Coarse-Graining of Dynamics

<sup>308</sup> The dependence of the matrices with respect to the displacements  $\mathbf{w}$  is dropped to isolate <sup>309</sup> the analysis based on coarsened variables. Consider a function of states in the form of <sup>310</sup>  $\mathbf{M}(\mathbf{u}) \mathbf{g}(\mathbf{u})$ , where  $\mathbf{g} : \mathbb{R}^{MP} \rightarrow \mathbb{R}^{MP}$  is a vector-valued function, and  $\mathbf{M} : \mathbb{R}^{MP} \rightarrow \mathbb{R}^{p \times MP}$  <sup>311</sup> is a matrix-valued function with an arbitrary dimension  $p$ . Define the projection matrix <sup>312</sup>  $\mathbf{P} = \boldsymbol{\Phi} \boldsymbol{\Phi}^+$  and the projection operator  $\mathcal{P}$  as,

$$\begin{aligned} \mathcal{P} [\mathbf{M}(\mathbf{u}) \mathbf{g}(\mathbf{u})] &= \mathbf{M}(\mathbf{P}\mathbf{u}) \mathbf{g}(\mathbf{P}\mathbf{u}) \\ &= \mathbf{M}(\boldsymbol{\Phi}\bar{\mathbf{u}}) \mathbf{g}(\boldsymbol{\Phi}\bar{\mathbf{u}}) \end{aligned} \quad (21)$$

<sup>313</sup> so that the resulting function depends only on the average temperatures  $\bar{\mathbf{u}}$ . Correspondingly, <sup>314</sup> the residual operator  $\mathcal{Q} = \mathcal{I} - \mathcal{P}$ , and  $\mathcal{Q} [\mathbf{M}(\mathbf{u}) \mathbf{g}(\mathbf{u})] = \mathbf{M}(\mathbf{u}) \mathbf{g}(\mathbf{u}) - \mathbf{M}(\boldsymbol{\Phi}\bar{\mathbf{u}}) \mathbf{g}(\boldsymbol{\Phi}\bar{\mathbf{u}})$ . When <sup>315</sup> the function is not separable, the projection operator is simply defined as  $\mathcal{P} [\mathbf{g}(\mathbf{u})] = \mathbf{g}(\mathbf{P}\mathbf{u})$ .

<sup>316</sup> Subsequently, the operators defined above are applied to coarse-grain the dynamics. First, <sup>317</sup> write the DG-FEM in eq. (7) as,

$$\dot{\mathbf{u}} = \mathbf{A}^{-1} \mathbf{B} \mathbf{u} + \mathbf{A}^{-1} \mathbf{C}(\mathbf{u}) \mathbf{u} + \mathbf{A}^{-1} \mathbf{f}(t) \quad (22)$$

<sup>318</sup> and multiply both sides by  $\boldsymbol{\Phi}^+$  to obtain,

$$\boldsymbol{\Phi}^+ \dot{\mathbf{u}} = \boldsymbol{\Phi}^+ (\boldsymbol{\Phi}\bar{\mathbf{u}} + \delta \mathbf{u}) = \dot{\bar{\mathbf{u}}} = \boldsymbol{\Phi}^+ \mathbf{r}(\mathbf{u}, t) \quad (23)$$

319 Apply the projection operator  $\mathcal{P}$  and the residual operator  $\mathcal{Q}$  to the right-hand side to obtain,

$$\dot{\bar{\mathbf{u}}} = \mathcal{P} [\Phi^+ \mathbf{r}(\mathbf{u}, t)] + \mathcal{Q} [\Phi^+ \mathbf{r}(\mathbf{u}, t)] \equiv \mathbf{r}^{(1)}(\bar{\mathbf{u}}, t) + \mathbf{r}^{(2)}(\mathbf{u}, t) \quad (24)$$

320 where  $\mathbf{r}^{(1)}(\bar{\mathbf{u}}, t)$  is resolved dynamics that depends on  $\bar{\mathbf{u}}$  only, and  $\mathbf{r}^{(2)}(\mathbf{u}, t)$  is the un-resolved  
321 or residual dynamics. Detailed derivations and analysis of  $\mathbf{r}^{(1)}(\bar{\mathbf{u}}, t)$  and  $\mathbf{r}^{(2)}(\mathbf{u}, t)$  can be  
322 found in the Appendix.

323 It follows from our previous work in Ref. [17] that the resolved dynamics is exactly the  
324 LCM, where the advection term reduces to zero, i.e.,  $\bar{\mathbf{C}}(\bar{\mathbf{u}}) = \mathbf{0}$ , as shown in the Appendix.  
325 Using the notation from eq. (11), it follows that,

$$\begin{aligned} \mathbf{r}^{(1)}(\bar{\mathbf{u}}, t) &= \bar{\mathbf{A}}(\mathbf{w})^{-1} \bar{\mathbf{B}}(\mathbf{w}) \bar{\mathbf{u}} + \bar{\mathbf{A}}(\mathbf{w})^{-1} \bar{\mathbf{C}}(\bar{\mathbf{u}}) \bar{\mathbf{u}} + \bar{\mathbf{A}}(\mathbf{w})^{-1} \bar{\mathbf{f}}(\bar{\mathbf{u}}) \\ &= \bar{\mathbf{A}}(\mathbf{w})^{-1} \bar{\mathbf{B}}(\mathbf{w}) \bar{\mathbf{u}} + \bar{\mathbf{A}}^{-1} \bar{\mathbf{f}}(t) \end{aligned} \quad (25)$$

326 where the following relations hold,

$$\bar{\mathbf{A}}(\mathbf{w}) = \mathbf{W} (\Phi^+ \mathbf{A}(\mathbf{w})^{-1} \Phi)^{-1} \quad \bar{\mathbf{C}}(\bar{\mathbf{u}}) = \mathbf{0} \quad (26a)$$

$$\bar{\mathbf{B}}(\mathbf{w}) = \mathbf{W} \Phi^+ \mathbf{B}(\mathbf{w}) \Phi \quad \bar{\mathbf{f}}(t) = \mathbf{W} \Phi^+ \mathbf{f} \quad (26b)$$

327 where  $\mathbf{W} \in \mathbb{R}^{N \times N}$  is a diagonal matrix with the  $i$ -th element as  $[\mathbf{W}]_{ii} = |\mathcal{V}_k|$  if  $i \in \mathcal{V}_k$ .  
328 The examination of the second residual term  $\mathbf{r}^{(2)}(\mathbf{u}, t)$  in eq. (24) is shown in the Appendix,  
329 and demonstrates that the physical sources of missing dynamics in the LCM include: the  
330 approximation of non-uniform temperature within each component as a constant, and the  
331 elimination of the advection term due to coarse-graining. In sum, the above results not  
332 only show that the LCM is a result of coarse-graining of the full-order DG-FEM, but also  
333 reveal the discrepancies between the LCM and the DG-FEM. These discrepancies propagate  
334 into the SRM, which as a result of the averaging in the LCM formulation, under-predicts  
335 the surface recession rates. In the subsequent section, the discrepancies in the LCM are  
336 corrected to formulate the PIROM.

### 337 3.2 Physics-Infusion Via Mori-Zwanzig Formalism

338 The Mori-Zwanzig (MZ) formalism is an operator-projection technique used to derive ROMs  
339 for high-dimensional dynamical systems, especially in statistical mechanics and fluid dy-  
340 namics [13, 14, 15]. It provides an exact reformulation of a high-dimensional Markovian dy-  
341 namical system, into a low-dimensional observable non-Markovian dynamical system. The  
342 proposed ROM is subsequently developed based on the approximation to the non-Markovian  
343 term in the observable dynamics. Particularly, eq. (24) shows that the DG-FEM dyna-  
344 mics can be decomposed into the resolved dynamics  $\mathbf{r}^{(1)}(\mathbf{u}, t)$  and the orthogonal dynamics  
345  $\mathbf{r}^{(2)}(\mathbf{u}, t)$ , in the sense of  $\mathcal{P}\mathbf{r}^{(2)} = 0$ . In this case, the MZ formalism can be invoked to ex-  
346 press the dynamics  $\bar{\mathbf{u}}$  in terms of  $\bar{\mathbf{u}}$  alone as the projected Generalized Langevin Equation  
347 (GLE) [13, 14, 15],

$$\dot{\bar{\mathbf{u}}}(t) = \mathbf{r}^{(1)}(\bar{\mathbf{u}}, t) + \int_0^t \tilde{\boldsymbol{\kappa}}(t, s, \bar{\mathbf{u}}) ds \quad (27)$$

348 where the first and second terms are referred to as the Markovian and non-Markovian terms,  
 349 respectively. The non-Markovian term accounts for the effects of past un-resolved states on  
 350 the current resolved states via a memory kernel  $\tilde{\kappa}(t, s, \bar{\mathbf{u}})$ , which in practice is computationally  
 351 expensive to evaluate.

### 352 3.2.1 Markovian Reformulation

353 This section details the formal derivation of the PIROM as a system of ODEs for the thermal  
 354 dynamics, based on approximations to the memory kernel. Specifically, the kernel  $\tilde{\kappa}$  is  
 355 examined via a leading-order expansion, based on prior work [19]; this can be viewed as an  
 356 analog of zeroth-order holding in linear system theory with a sufficiently small time step. In  
 357 this case, the memory kernel is approximated as,

$$\tilde{\kappa}(t, s, \bar{\mathbf{u}}) \approx \mathbf{r}^{(1)}(\bar{\mathbf{u}}, t) \cdot \nabla_{\bar{\mathbf{u}}} \mathbf{r}^{(2)}(\Phi \bar{\mathbf{u}}, t) \quad (28)$$

358 Note that the terms in  $\mathbf{r}^{(1)}$  have a common factor  $\bar{\mathbf{A}}^{-1}$ ; this motivates the following heuristic  
 359 modification of the model form in eq. (27),

$$\dot{\bar{\mathbf{u}}} = \mathbf{r}^{(1)}(\bar{\mathbf{u}}, t) + \bar{\mathbf{A}}(\mathbf{w})^{-1} \int_0^t \kappa(t, s, \bar{\mathbf{u}}) ds \quad (29a)$$

$$\bar{\mathbf{A}}(\mathbf{w}) \dot{\bar{\mathbf{u}}} = \bar{\mathbf{B}}(\mathbf{w}) \bar{\mathbf{u}} + \bar{\mathbf{f}}(t) + \int_0^t \kappa(t, s, \bar{\mathbf{u}}) ds \quad (29b)$$

360 where the original kernel  $\tilde{\kappa}$  is effectively normalized by  $\bar{\mathbf{A}}(\mathbf{w})^{-1}$ . Intuitively, such choice  
 361 of kernel reduces its dependency on the averaged material properties, and simplifies the  
 362 subsequent design of model form.

363 Subsequently, the hidden states are introduced to “Markovianize” the system eq. (27).  
 364 In this manner, eq. (29b) is converted into a pure state-space model, with the functional  
 365 form of the LCM retained; since LCM is a physics-based model, then it encodes the phys-  
 366 ical information and retains explicit parametric dependence of the problem. Consider the  
 367 representation of the kernel as a finite sum of simpler functions, e.g., exponentials,

$$\kappa(t, s, \bar{\mathbf{u}}) = \sum_{j=1}^m \mathcal{K}_j(t, s, \bar{\mathbf{u}}) [\mathbf{p}_j + \mathbf{d}_j(\bar{\mathbf{u}})] \phi_j(s, \bar{\mathbf{u}}) \quad (30)$$

368 where,

$$\mathcal{K}_j(t, s, \bar{\mathbf{u}}) = e^{-\int_s^t (\lambda_j + e_j(\bar{\mathbf{u}})) d\tau}, \quad \phi_j(s, \bar{\mathbf{u}}) = \mathbf{q}_j^\top \bar{\mathbf{u}}(s) + \mathbf{g}_j(\bar{\mathbf{u}})^\top \bar{\mathbf{u}}(s) + \mathbf{r}_j^\top \bar{\mathbf{f}}(s) \quad (31)$$

369 with suitable coefficients  $\mathbf{p}_j, \mathbf{d}_j, \mathbf{q}_j, \mathbf{g}_j, \mathbf{r}_j \in \mathbb{R}^N$  and decay rates  $\lambda_j, e_j(\bar{\mathbf{u}}) > 0$ , that need to  
 370 be identified from data.

371 Define the hidden states as,

$$\beta_j(t) = \int_0^t \mathcal{K}_j(s, \bar{\mathbf{u}}) \phi_j(s, \bar{\mathbf{u}}) ds \quad (32)$$

<sup>372</sup> and differentiate with respect to time,,

$$\dot{\beta}_j(t) = -[\lambda_j + e_j(\bar{\mathbf{u}})]\beta_j(t) + \mathbf{q}_j^\top \bar{\mathbf{u}}(t) + \mathbf{g}_j(\bar{\mathbf{u}})^\top \bar{\mathbf{u}}(t) + \mathbf{r}_j^\top \bar{\mathbf{f}}(t) \quad (33)$$

<sup>373</sup> to obtain the memory,

$$\int_0^t \boldsymbol{\kappa}(t, s, \bar{\mathbf{u}}) ds = \sum_{j=1}^m [\mathbf{p}_j + \mathbf{d}_j(\bar{\mathbf{u}})] \beta_j(t) \quad (34)$$

<sup>374</sup> Then, eq. (29b) is recast as the extended Markovian system,

$$\bar{\mathbf{A}}(\mathbf{w})\dot{\bar{\mathbf{u}}} = \bar{\mathbf{B}}(\mathbf{w})\bar{\mathbf{u}} + [\mathbf{P} + \mathbf{D}(\bar{\mathbf{u}})]\boldsymbol{\beta} + \bar{\mathbf{f}}(t) \quad (35a)$$

$$\dot{\boldsymbol{\beta}} = [\mathbf{Q} + \mathbf{G}(\bar{\mathbf{u}})]\bar{\mathbf{u}} + [\mathbf{E}(\bar{\mathbf{u}}) - \boldsymbol{\Lambda}]\boldsymbol{\beta} + \mathbf{R}\bar{\mathbf{f}}(t) \quad (35b)$$

<sup>375</sup> where the data-driven operators associated to the hidden dynamics are collected as,

$$\boldsymbol{\Lambda} = \text{diag}[\lambda_1, \lambda_2, \dots, \lambda_m] \in \mathbb{R}^{m \times m}, \quad \mathbf{P} = [\mathbf{p}_1, \mathbf{p}_2, \dots, \mathbf{p}_m] \in \mathbb{R}^{N \times m} \quad (36a)$$

$$\mathbf{D}(\bar{\mathbf{u}}) = [\mathbf{d}_1(\bar{\mathbf{u}}), \mathbf{d}_2(\bar{\mathbf{u}}), \dots, \mathbf{d}_m(\bar{\mathbf{u}})] \in \mathbb{R}^{N \times m}, \quad \mathbf{Q} = [\mathbf{q}_1, \mathbf{q}_2, \dots, \mathbf{q}_m] \in \mathbb{R}^{m \times N} \quad (36b)$$

$$\mathbf{G}(\bar{\mathbf{u}}) = [\mathbf{g}_1(\bar{\mathbf{u}}), \mathbf{g}_2(\bar{\mathbf{u}}), \dots, \mathbf{g}_m(\bar{\mathbf{u}})] \in \mathbb{R}^{m \times N}, \quad \mathbf{R} = [\mathbf{r}_1, \mathbf{r}_2, \dots, \mathbf{r}_m] \in \mathbb{R}^{m \times N} \quad (36c)$$

$$\mathbf{E}(\bar{\mathbf{u}}) = \text{diag}[e_1(\bar{\mathbf{u}}), e_2(\bar{\mathbf{u}}), \dots, e_m(\bar{\mathbf{u}})] \in \mathbb{R}^{m \times m} \quad (36d)$$

<sup>376</sup> The form of the temperature-dependent matrices  $\mathbf{D}(\bar{\mathbf{u}})$ ,  $\mathbf{G}(\bar{\mathbf{u}})$ , and  $\mathbf{E}(\bar{\mathbf{u}})$  is specified in the  
<sup>377</sup> next section. Since the hidden states  $\boldsymbol{\beta}$  serve as the memory, their initial conditions are set  
<sup>378</sup> to zero, i.e.,  $\boldsymbol{\beta}(t_0) = \mathbf{0}$ , no memory at the beginning. The physics-infused model in eq. (35)  
<sup>379</sup> retains the structure of the LCM and depend on the displacements  $\mathbf{w}$ , while the hidden states  
<sup>380</sup> account for missing physics through corrections to the stiffness and advection matrices, as  
<sup>381</sup> well as the forcing term.

### <sup>382</sup> 3.2.2 Coupled Physics-Infused Model

<sup>383</sup> The next step involves coupling the physics-infused model in eq. (35) with the SRM in  
<sup>384</sup> eq. (10) to define the PIROM for ablating TPS. To this end, define the surface temperature  
<sup>385</sup>  $\mathbf{z}_u \in \mathbb{R}^{\tilde{N}}$  and displacements  $\mathbf{z}_w \in \mathbb{R}^{\tilde{N}}$  for  $\tilde{N} \leq N$  ablating components so that the observable  
<sup>386</sup> is given by  $\mathbf{z} = [\mathbf{z}_u, \mathbf{z}_w]^\top \in \mathbb{R}^{n_z}$  with  $n_z = 2\tilde{N}$  as the total number of observables.

<sup>387</sup> Collect the RPM and hidden states into a single state vector  $\mathbf{y} = [\bar{\mathbf{u}}, \mathbf{w}, \boldsymbol{\beta}]^\top \in \mathbb{R}^{n_y}$ , where  
<sup>388</sup>  $n_y = N + \tilde{N} + m$ , and define a data-driven operator  $\mathbf{M} \in \mathbb{R}^{n_z \times n_y}$  to define the PIROM's  
<sup>389</sup> observable as,

$$\mathbf{z} = \mathbf{My} \quad (37)$$

<sup>390</sup> where,

$$\mathbf{M} = \begin{bmatrix} \mathbf{M}_{\bar{u}} & \mathbf{0} & \mathbf{M}_{\boldsymbol{\beta}} \\ \mathbf{0} & \mathbf{I} & \mathbf{0} \end{bmatrix} \quad (38)$$

<sup>391</sup> includes the matrices  $\mathbf{M}_{\bar{u}} \in \mathbb{R}^{\tilde{N} \times N}$  and  $\mathbf{M}_{\boldsymbol{\beta}} \in \mathbb{R}^{\tilde{N} \times m}$ , which computes the surface tempera-  
<sup>392</sup> ture observable from the RPM states and hidden states, respectively. The PIROM is coupled  
<sup>393</sup> to the SRM in eq. (10) by leveraging eq. (37) to compute the surface recession velocity. Thus,

<sup>394</sup> the PIROM is formally stated as,

$$\mathcal{A}\dot{\mathbf{y}} = [\mathcal{B} + \mathcal{C}] \mathbf{y} + \mathcal{F}(t) \quad (39a)$$

$$\mathbf{z} = \mathbf{M}\mathbf{y} \quad (39b)$$

<sup>395</sup> where,

$$\mathcal{A} = \begin{bmatrix} \bar{\mathbf{A}}(\mathbf{w}) & \mathbf{O} & \mathbf{O} \\ \mathbf{O} & \mathbf{I} & \mathbf{O} \\ \mathbf{O} & \mathbf{O} & \mathbf{I} \end{bmatrix} \in \mathbb{R}^{n_y \times n_y}, \quad \mathcal{B} = \begin{bmatrix} \bar{\mathbf{B}}(\mathbf{w}) & \mathbf{O} & \mathbf{P} \\ \Xi\mathbf{M}_u & \mathbf{O} & \Xi\mathbf{M}_\beta \\ \mathbf{Q} & \mathbf{O} & -\Lambda \end{bmatrix} \in \mathbb{R}^{n_y \times n_y}, \quad (40a)$$

$$\mathcal{C} = \begin{bmatrix} \mathbf{O} & \mathbf{O} & \mathbf{D}(\bar{\mathbf{u}}) \\ \mathbf{O} & \mathbf{O} & \mathbf{O} \\ \mathbf{G}(\bar{\mathbf{u}}) & \mathbf{O} & \mathbf{E}(\bar{\mathbf{u}}) \end{bmatrix} \in \mathbb{R}^{n_y \times n_y}, \quad \mathcal{F} = \begin{bmatrix} \bar{\mathbf{f}}(t) \\ -\tilde{\mathbf{f}} \\ \mathbf{R}\bar{\mathbf{f}}(t) \end{bmatrix} \in \mathbb{R}^{n_y} \quad (40b)$$

<sup>396</sup> The learnable parameters in the PIROM are collected as,

$$\Theta = \{\mathbf{P}, \Lambda, \mathbf{Q}, \mathbf{M}, \mathbf{D}(\bar{\mathbf{u}}), \mathbf{G}(\bar{\mathbf{u}}), \mathbf{E}(\bar{\mathbf{u}}), \mathbf{R}\}, \in \mathbb{R}^{n_\theta} \quad (41)$$

<sup>397</sup> The matrices  $\mathbf{P}, \Lambda, \mathbf{Q}, \mathbf{M}, \mathbf{R}$  are constants, and account for the effects of coarse-graining on  
<sup>398</sup> the stiffness, output, and forcing matrices. The matrices  $\mathbf{D}(\bar{\mathbf{u}}), \mathbf{E}(\bar{\mathbf{u}}), \mathbf{G}(\bar{\mathbf{u}})$  are temperature-  
<sup>399</sup> dependent matrices, and account for the effects of coarse-graining on the advection matrix  
<sup>400</sup> due to mesh motion. Leveraging the DG-FEM formula for the advection matrix in eq. (56c)  
<sup>401</sup> in the Appendix, and noting that the ablating velocity in eq. (4) imposes the boundary  
<sup>402</sup> condition for the mesh motion, the state-dependent matrices for the  $i$ -th component are  
<sup>403</sup> written as,

$$\mathbf{D}(\bar{\mathbf{u}}) \approx \text{diag}[\dot{\mathbf{w}}] \mathbf{D}, \quad \mathbf{G}(\bar{\mathbf{u}}) \approx \mathbf{G} \text{diag}[\dot{\mathbf{w}}], \quad \mathbf{E}(\bar{\mathbf{u}}) \approx \text{diag} \left[ \underbrace{\dot{\mathbf{w}}, \dots, \dot{\mathbf{w}}}_{\tilde{m} \text{ times}} \right] \mathbf{E} \quad (42)$$

<sup>404</sup> where  $\dot{\mathbf{w}} = \dot{\mathbf{w}}(\bar{\mathbf{u}})$  is the SRM based on the observable temperature  $\bar{\mathbf{u}}$  and  $\tilde{m}$  is the number  
<sup>405</sup> of hidden states per component so that  $m = N\tilde{m}$ .

<sup>406</sup> The PIROM in eq. (39) incorporates explicit information on the material properties,  
<sup>407</sup> boundary conditions, and surface recession, and is designed to generalize across parametric  
<sup>408</sup> variations in these inputs. Moreover, the hidden dynamics in eq. (35) are interpretable, as  
<sup>409</sup> these retain the functional form of the DG-FEM in eq. (7). The next step is focused on  
<sup>410</sup> identifying the unknown data-driven parameters  $\Theta$  characterizing the hidden dynamics.

### <sup>411</sup> 3.3 Learning the Hidden Dynamics

<sup>412</sup> Learning of the PIROM is achieved through a gradient-based neural-ODE-like approach [3].  
<sup>413</sup> For ease of presentation, consider the compact form of the PIROM in eq. (39),

$$\mathcal{D}(\dot{\mathbf{y}}, \mathbf{y}, \xi, \mathcal{F}; \Theta) = \mathbf{0} \quad (43)$$

<sup>414</sup> where  $\boldsymbol{\xi}$  defines the model parameters, i.e., material properties and B' tables, while  $\mathcal{F}$ <sup>415</sup> represents the forcing terms, i.e., the boundary conditions.

<sup>416</sup> Consider a dataset of  $N_s$  high-fidelity *surface temperature* observable trajectories  $\mathbf{z}_{\text{HF}}$ ,<sup>417</sup> sampled at  $p$  time instances  $\{t_k\}_{k=0}^{p-1}$ , for different parameter settings  $\{\boldsymbol{\xi}^{(l)}\}_{l=1}^{N_s}$  and forcing<sup>418</sup> functions  $\{\mathcal{F}^{(l)}(t)\}_{l=1}^{N_s}$ . The dataset is expressed as,

$$\mathcal{D} = \left\{ \left( t_k, \mathbf{z}_{\text{HF}}^{(l)}(t_k), \boldsymbol{\xi}^{(l)}, \mathcal{F}^{(l)}(t_k) \right) \right\}_{l=1}^{N_s}, \quad k = 0, 1, \dots, p-1 \quad (44)$$

<sup>419</sup> In this work, the dataset contains only surface temperature observables – all high-fidelity<sup>420</sup> information regarding the surface displacements *are assumed to be unavailable during learning*.<sup>421</sup>

<sup>422</sup> The learning problem is formulated as the following differentially-constrained problem,

$$\min_{\Theta} \quad \mathcal{J}(\Theta; \mathcal{D}) = \sum_{l=1}^{N_s} \int_{t_0}^{t_f} \ell \left( \mathbf{z}_u^{(l)}, \mathbf{z}_{\text{HF}}^{(l)} \right) dt \quad (45a)$$

$$\text{s.t.} \quad \mathbf{0} = \mathcal{D} \left( \dot{\mathbf{y}}^{(l)}, \mathbf{y}^{(l)}, \boldsymbol{\xi}^{(l)}, \mathcal{F}^{(l)}; \Theta \right) \quad (45b)$$

<sup>423</sup> for  $l = 1, 2, \dots, N_s$ , the objective is to minimize the discrepancy between the high-fidelity<sup>424</sup> and PIROM predictions for the  $l$ -th trajectory with  $\ell \left( \mathbf{z}_u^{(l)}, \mathbf{z}_{\text{HF}}^{(l)} \right) = \left\| \mathbf{z}_u^{(l)} - \mathbf{z}_{\text{HF}}^{(l)} \right\|_2^2$ .

<sup>425</sup> The gradient-based optimization loop is based on the adjoint variable  $\boldsymbol{\lambda}$ , governed by the<sup>426</sup> adjoint differential equation,

$$\frac{\partial \ell}{\partial \mathbf{y}} + \boldsymbol{\lambda}^\top \frac{\partial \mathcal{D}}{\partial \mathbf{y}} - \frac{d}{dt} \left( \boldsymbol{\lambda}^\top \frac{\partial \mathcal{D}}{\partial \dot{\mathbf{y}}} \right) = \mathbf{0} \quad (46a)$$

$$\boldsymbol{\lambda}(t_f)^\top \frac{\partial \mathcal{D}}{\partial \dot{\mathbf{y}}(t_f)} = \mathbf{0} \quad (46b)$$

<sup>427</sup> Once  $\boldsymbol{\lambda}$  is solved, the gradient is computed as,

$$\nabla_\Theta \mathcal{J} = \frac{1}{N_s} \sum_{l=1}^{N_s} \int_{t_0}^{t_f} \left( \frac{\partial \ell}{\partial \Theta} + \left( \boldsymbol{\lambda}^{(l)} \right)^\top \frac{\partial \mathcal{D}}{\partial \Theta} \right) dt \quad (47)$$

## <sup>428</sup> 4 Application to Thermal Protection Systems

<sup>429</sup> In this section, the proposed PIROM approach is applied to the analysis of thermo-ablative<sup>430</sup> multi-layered hypersonic TPS. The performance of the PIROM is evaluated in terms of the<sup>431</sup> three corners of the ITM in Fig. 1, based on parametric variations of boundary conditions and<sup>432</sup> SRMs. The results show PIROM to be a promising candidate for the solution of the impossible<sup>433</sup> trinity of modeling, achieving RPM-level computational efficiency and generalizability,<sup>434</sup> while attaining high-fidelity model accuracy.

Component	$w$ (cm)	$h$ (cm)	$\rho$ (kg/m <sup>3</sup> )	$c_p$ (J/kg·K)	$k$ (W/m·K)	$\alpha \times 10^{-6}$ (m/s·K)
#1	0.3	0.03	160	1200	0.2	1
#2	0.3	0.03	1800	900	5	1
#3	0.3	0.03	300	1500	0.15	1
#4	0.9	0.03	1600	800	10	0

Table 1: Description of TPS components, including thickness  $h$ , density  $\rho$ , specific heat capacity  $c_p$ , thermal conductivity  $k$ , and SRM parameter  $\alpha$ .

## 4.1 Problem Definition

Consider the two-dimensional TPS configuration shown in Fig. 3 with constant material properties within each layer, dimensions, and BCs listed in Table 1. Such configuration is representative of the TPS used for the initial concept 3.X vehicle in past studies [10], and involves two main layers: an outer ablative layer, and an inner substrate layer. The top ablative layer may be composed of different materials, such as PICA or Avcoat, while the substrate layer is typically made of a high-temperature resistant material, such as carbon-carbon composite [7]. The ablative layer, composed of  $\tilde{N} = 3$  ablative components, is subjected to strong time-varying and non-uniform heating, while the substrate layer, composed of one non-ablative component, is insulated adiabatically at the outer surface; the total number of components is thus  $N = 4$ .

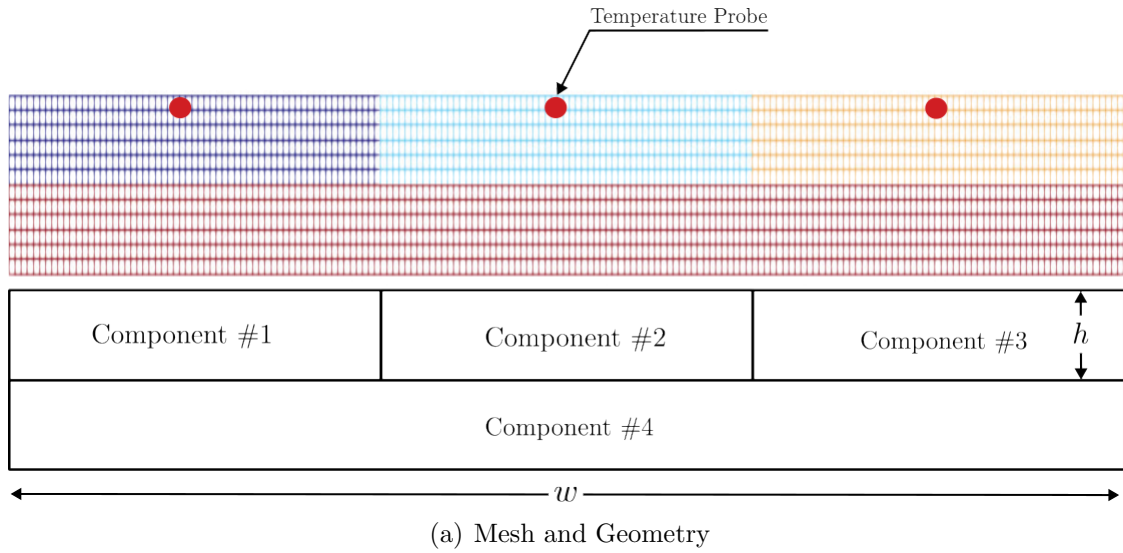
The lumped-mass representation of the TPS configuration is shown in Fig. 3(b), where each component  $\Omega_i$  is represented by a lumped mass with uniform temperature  $u_i(t)$ . Details regarding the derivation of the LCM for this configuration are provided in Appendix A. The sources of non-linearities studied in this problem originate from the coupling between the thermodynamics and temperature-dependent mesh motion, i.e., geometry-dependent matrices, as well as the heterogeneities across material layers. As shown in Fig. 3, perfect thermocouple devices are placed at the surfaces of the ablative layers for the collection of the high-fidelity temperature signals that are used in the following sections for training and testing the PIROM.

## 4.2 Problem Parametrization

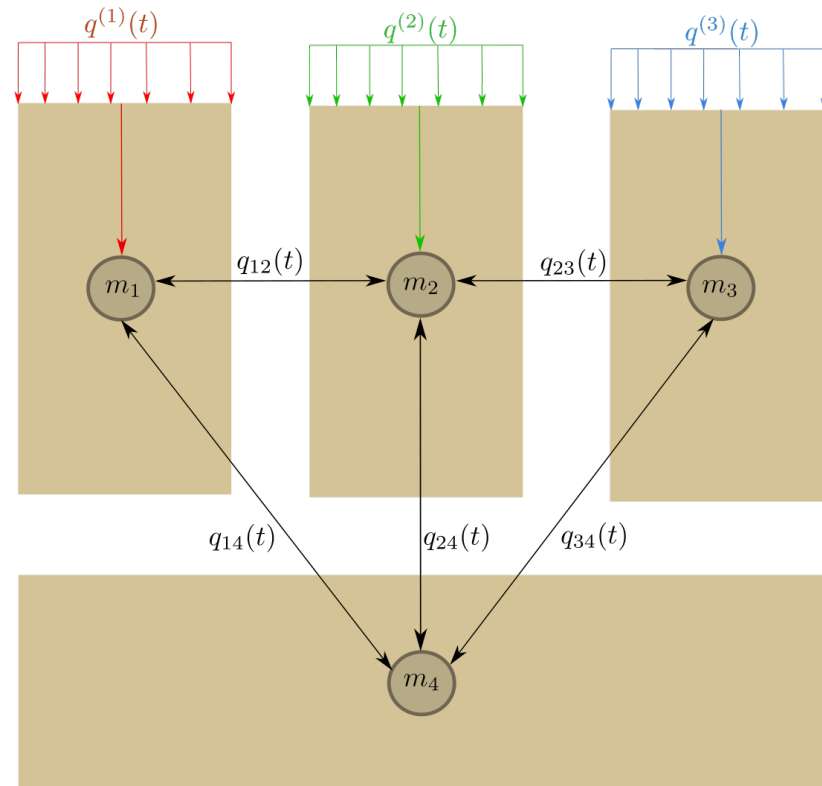
The operating conditions of the TPS are specified by the boundary conditions, i.e., the heat flux, and the surface recession model (SRM). Specifically, the heat flux on the Neumann BC is parametrized using  $\boldsymbol{\xi}_{\text{BC}} = \{\xi_0, \xi_1, \xi_2\}$ , while the SRM is parametrized using  $\boldsymbol{\xi}_{\text{SRM}} = \{\alpha_1, \alpha_2, \alpha_3\}$ . Thus, the heat flux and SRM over the  $i$ -th ablative component are expressed as,

$$q_i(x, t; \boldsymbol{\xi}_{\text{BC}}) = \xi_0 e^{\xi_1 x} e^{\xi_2 t}, \quad \forall x \in \Gamma_{i,q}, \quad \dot{w}_i(z_{u,i}; \boldsymbol{\xi}_{\text{SRM}}) = \alpha_i (z_{u,i} - u_{0,i}), \quad i = 1, \dots, \tilde{N} \quad (48)$$

where  $\Gamma_{i,q}$ ,  $z_{u,i}$ , and  $u_{0,i}$  correspond to the Neumann BC surface, the PIROM's surface temperature prediction, and the initial temperature of the  $i$ -th ablative component, respectively. The parameters  $\xi_0$ ,  $\xi_1$ , and  $\xi_2$  control the heat flux magnitude, spatial variation, and temporal variation, respectively. The constant  $\alpha_i$  is a small material-dependent constant determined



(a) Mesh and Geometry



(b) Lumped Mass Representation

Figure 3: Four-component TPS geometry and lumped-mass representation for the TPS.

465 from the B' table [12], specifying the surface recession velocity for a given temperature.

### 466 4.3 Data Generation

467 Full-order solutions of the TPS are computed using the FEM multi-mechanics module from  
468 the **Aria** package [4], where the mesh is shown in Fig. 3. The mesh consists of 2196 total  
469 elements, with 366 elements for each ablative component and 1098 elements for the sub-  
470 strate component. Given an operating condition  $\xi = [\xi_{\text{BC}}, \xi_{\text{SRM}}]^\top$ , a high-fidelity solution  
471 is computed for one minute, starting from an uniform initial temperature of  $T(x, t_0) = 300$   
472 K. Each solution consist of a collection of space-time-varying temperature and displacement  
473 fields  $\left\{ \left( t_k, \mathbf{u}_{\text{HF}}^{(l)}(t_k), \mathbf{d}_{\text{HF}}^{(l)}(t_k), \xi^{(l)} \right) \right\}_{k=0}^{p-1}$ , where  $p$  is the number of time steps with a step size of  
474  $\Delta t \approx 10^{-3}$ . The observable trajectories are representative of near-wall thermocouple sensing  
475 of hypersonic flows involving heat transfer. At each time instance  $t_k$ , a temperature reading  
476 is recorded from each ablative component using the thermocouples shown in Fig. 3, resulting  
477 in three temperature signals, i.e., the observables  $\mathbf{z}_{\text{HF}} \in \mathbb{R}^3$ . Therefore, each full-order solu-  
478 tion produces one trajectory of observables  $\left\{ \left( t_k, \mathbf{z}_{\text{HF}}^{(l)}(t_k), \xi^{(l)} \right) \right\}_{k=0}^{p-1}$ . The goal of the PIROM  
479 is to predict the surface temperature and displacement as accurately as possible.

#### 480 4.3.1 Definition of Training and Testing Datasets

481 The range of parameters used to generate the training  $\mathcal{D}_1$  and testing  $\{\mathcal{D}_2, \mathcal{D}_3\}$  datasets  
482 are listed in Table 1. The training and testing datasets are designed, respectively, to: (1)  
483 minimize the information that the PIROM can “see”, and (2) to maximize the variabil-  
484 ity of test operating conditions to examine the PIROM’s generalization performance. A  
485 total of 110 normally-distributed data points for the BC parametrization are visualized in  
486 Fig. 4(a), and the corresponding observable trajectories are shown in Figs. 4(b) and 4(c).  
487 The training dataset  $\mathcal{D}_1$  includes 10 trajectories with randomly selected BC parameters from  
488 the 110 points, with nominal SRM parameters  $\xi_{\text{SRM}} = \{1, 1, 1\} \times 10^{-6}$ . Note that although  
489 Fig. 4(c) shows the surface displacements for all ablative components in  $\mathcal{D}_1$ , only the *surface*  
490 *temperature is used for training the PIROM.*

491 Two additional datasets are generated for testing. The dataset  $\mathcal{D}_2$  includes the remaining  
492 100 BC parameter values not considered in  $\mathcal{D}_1$ , and the high-fidelity simulation are generated  
493 with the same nominal SRM parameters. The cases in the  $\mathcal{D}_3$  fixes the boundary condition  
494 as shown in Fig. 4(a) and varies the SRM parameters as shown in Table. 1. The testing  
495 datasets  $\mathcal{D}_2$  and  $\mathcal{D}_3$  are *out-of-distribution* (OOD) datasets, and are meant for testing the  
496 generalizability of the ROMs to unseen BCs and SRMs, respectively.

### 497 4.4 Performance Metrics

498 The performance of the PIROM is evaluated by the metrics of prediction error and computa-  
499 tinoal cost.

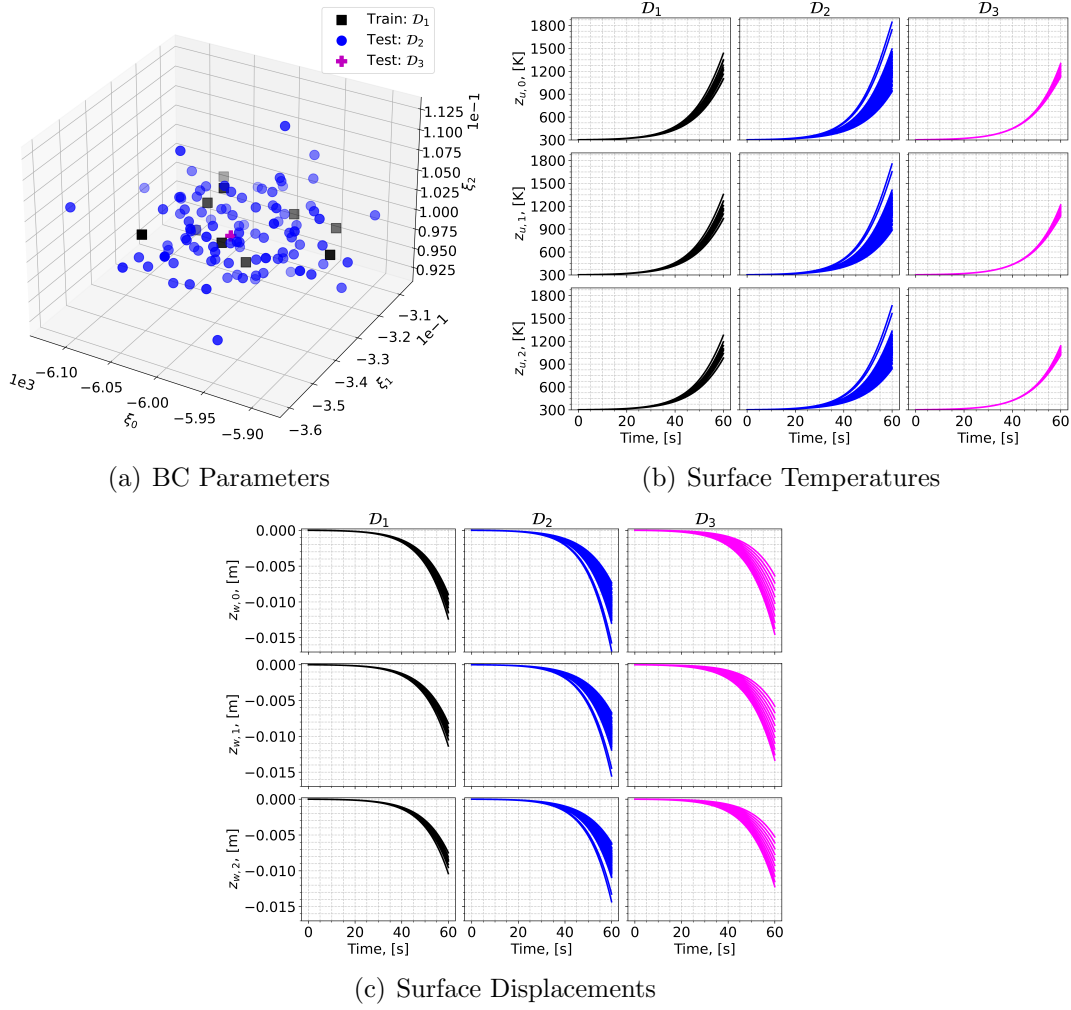


Figure 4: Boundary condition parameters, temperature observables, and displacement observables for the training and testing datasets. The variables  $z_{u,i}$  and  $z_{w,i}$  correspond to the surface temperature and displacement of the  $i$ -th ablative component, respectively.

500 **Prediction Error** Consider one trajectory of high-fidelity surface temperature and dis-  
 501 placement data  $\left\{ \left( t_k, \mathbf{z}_{u,\text{HF}}^{(l)}(t_k), \mathbf{z}_{w,\text{HF}}^{(l)}(t_k) \right) \right\}_{k=0}^{p-1}$  for the  $l$ -th operating condition in the testing  
 502 datasets  $\mathcal{D}_2$  or  $\mathcal{D}_3$ . The difference  $e_i^{(l)}$  for the  $i$ -th predicted observable, denoted as  $z_i^{(l)}$ , is  
 503 computed as,

$$e_i^{(l)} = \frac{1}{\Delta z_i^{(l)}} \sqrt{\frac{1}{p} \sum_{k=0}^{p-1} \left( z_{i,\text{HF}}^{(l)}(t_k) - z_i^{(l)}(t_k) \right)^2} \quad (49)$$

504 for  $i = 1, 2, 3$  and  $z_i^{(l)} \in \{z_{i,u}^{(l)}, z_{i,w}^{(l)}\}$ , and where,

$$\Delta z_i^{(l)} = \max_{0 \leq k \leq p-1} z_{i,\text{HF}}^{(l)}(t_k) - \min_{0 \leq k \leq p-1} z_{i,\text{HF}}^{(l)}(t_k) \quad (50)$$

505 Subsequently, the prediction error of one trajectory is computed by a weighted sum based  
 506 on the area of each *ablative component*, resulting in the normalized root mean square error  
 507 (NRMSE) metric for one trajectory,

$$\text{NRMSE} = \frac{\sum_{i=1}^{\tilde{N}} |\Omega_i| e_i^{(l)}}{\sum_{i=1}^{\tilde{N}} |\Omega_i|} \times 100\% \quad (51)$$

508 For one dataset, the NRMSE is defined to be the average of the NRMSEs of all trajectories  
 509 in the dataset.

510 **Computational Acceleration** The *computational acceleration* metric focuses on the quan-  
 511 tification of the speedup factor  $\frac{\mathcal{T}_{\text{HF}}(\mathcal{D})}{\mathcal{T}_{\mathcal{M}}(\mathcal{D})}$ , where  $\mathcal{T}_{\text{HF}}(\mathcal{D})$  and  $\mathcal{T}_{\mathcal{M}}(\mathcal{D})$  correspond to the wall-clock  
 512 time required by the high-fidelity model and the reduced-order model  $\mathcal{M}$  (i.e., PIROM or  
 513 RPM) to evaluate all trajectories in the dataset  $\mathcal{D}$ , respectively. For a benchmark analysis  
 514 of the computational costs during the training phase, please refer to Ref. [17].

## 515 4.5 Generalization to Boundary Conditions

516 To assess generalization to BC, the PIROM and RPM are evaluated on the  $\mathcal{D}_2$  dataset. Tem-  
 517 perature trajectory predictions for a representative test case are shown in Figs. 5(a) and 5(b),  
 518 where the PIROM accurately captures the surface temperature and displacement dynamics,  
 519 while the RPM exhibits larger deviations and under-predicts surface displacements due to  
 520 the averaging effects of the LCM. The mean NRMSE across all test cases in  $\mathcal{D}_2$  is shown  
 521 in Figs. 5(e) and 5(f), where the PIROM consistently achieves errors of  $\approx 0.5\%$  for both  
 522 temperature and displacement predictions, improving the RPM's accuracy by an order of  
 523 magnitude. Figure 5 reports the average substrate temperature, where the LCM remains  
 524 highly accurate due to the symmetric TPS geometry, adiabatic BCs, and negligible thermal  
 525 gradients within the substrate. Although the PIROM is trained only on the surface tem-  
 526 peratures of the three ablative components, its hidden dynamics retain the LCM's accuracy  
 527 for this untrained observable, demonstrating the PIROM's ability to generalize and preserve  
 528 the underlying physics of the reduced-physics backbone.

529 **4.6 Generalization to Surface Recession Models**

530 The generalization performance of the PIROM and RPM is also evaluated on surface recess-  
531 sion models using the  $\mathcal{D}_3$  dataset. As detailed in Table 1, the SRM parameter  $\alpha$  in  $\mathcal{D}_3$  is  
532 perturbed 10 times by up to  $\pm 50\%$  from their nominal values. The SRM model perturbation  
533 introduces significant changes to the ablative layer dynamics, potentially increasing the rate  
534 of ablation at lower temperatures, as shown in Figs. 5(c) and 5(d). The PIROM, without  
535 considering any SRM variations during training, is able to accurately predict the surface tem-  
536 perature and displacement dynamics for the perturbed SRMs. Figures 5(e) and 5(f) show  
537 the mean NRMSE across all test cases in  $\mathcal{D}_3$ , where the PIROM consistently achieves errors  
538 below 1.5% for both temperature and displacement predictions, and consistently improves  
539 the RPM’s accuracy by approximately an order of magnitude.

540 **4.7 Computational Cost**

541 All computations are performed in serial for fairness on an Intel Xeon (R) Gold 6258R  
542 CPU 2.70GHz computer with 62 GB of RAM. The numerical integration for the RPM  
543 and PIROM models are performed using SciPy’s `solve_ivp` function with default settings.  
544 Provided a parametrization for the BC and SRM, the high-fidelity FEM simulation takes  
545 about  $\approx 60$  seconds, the RPM takes about  $\approx 0.137$  seconds, and the PIROM takes about  
546  $\approx 0.280$  seconds. Therefore, during evaluation both the RPM and PIROM achieve speedup  
547 factors of approximately 438 and 214, respectively, over the high-fidelity model. As a result,  
548 the PIROM and RPM are *two-orders-of-magnitude faster* than the high-fidelity model. The  
549 PIROM nearly preserves the computational efficiency of the RPM (about twice as expensive  
550 as the RPM), while achieving significantly higher accuracy and generalization capabilities.  
551 The results demonstrate the benefits of physics-infused modeling for the development of  
552 efficient and generalizable ROMs for complex multi-physics systems.

553 **4.8 Summary of Results**

554 The results presented in this section demonstrate the accuracy, generalizability, and com-  
555 putational efficiency of the proposed PIROM approach for the analysis of thermo-ablative  
556 multi-layered hypersonic TPS. The PIROM consistently achieves low prediction errors below  
557 1% for both surface temperature and displacement across a range of unseen boundary con-  
558 ditions and surface recession models. Furthermore, the PIROM retains the computational  
559 efficiency of traditional RPMs, achieving speedup factors of over 200 times compared to high-  
560 fidelity FEM simulations. The generalization capabilities of the PIROM are attributed to its  
561 hybrid structure: a physics-based LCM backbone that ensures consistency with the under-  
562 lying thermodynamics, while a data-driven correction mechanism captures the un-resolved  
563 dynamics.

564 **5 Conclusions**

565 This work presents the development and validation of the *scientific machine learning* frame-  
566 work termed *Physics-Informed Reduced Order Model* (PIROM) for simulating the transient

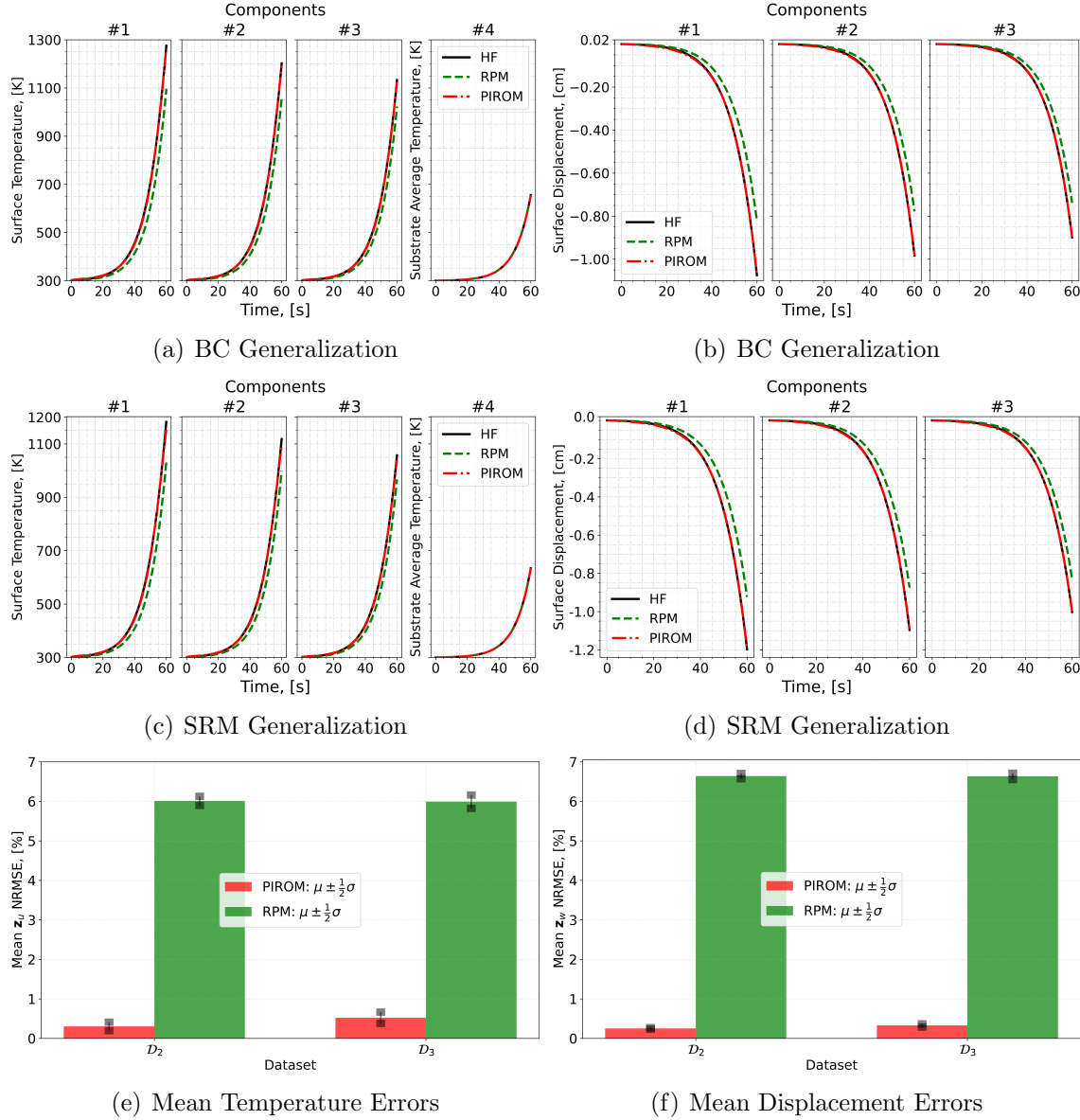


Figure 5: PIROM predictions against high-fidelity solutions for (a)-(b) BC generalization, (c)-(d) SRM generalization, and (e)-(f) mean errors across testing datasets.

567 thermo-ablative response of hypersonic thermal protection systems (TPS) subjected to hy-  
568 personic aerodynamic heating. Using coarse-graining on a DG-FEM model and the Mori-  
569 Zwanzig formalism, the PIROM formulation in Ref. [17] is extended to account for non-  
570 decomposing ablative material response. The PIROM builds upon the following two key  
571 components: (1) a first-order physics-based model, i.e., the LCM and SRM, for low-fidelity  
572 predictions of the transient thermo-ablative TPS response; and (2) a data-driven closure to  
573 the non-Markovian term in the generalized Langevin equation (GLE). The non-Markovian  
574 closure is recast as a set of hidden states that evolve according to a data-driven dynamical  
575 system that is learned from a sparse collection of high-fidelity temperature signals.

576 The results demonstrate that the PIROM framework effectively reconciles the trade-  
577 offs between accuracy, generalizability, and efficiency of the ITM for simulating ablating  
578 hypersonic TPS. The PIROM consistently achieves mean observable prediction errors of  
579  $\approx 0.5\%$  for a wide range of extrapolative settings of model parameters, involving time-and-  
580 space varying boundary conditions and SRM models. Notably, the PIROM improves the  
581 RPM's accuracy by an order of magnitude while preserving its computational efficiency,  
582 physical interpretability, and parametric generalizability. Moreover, the PIROM delivers  
583 online evaluations that are two orders of magnitude faster than the FOM. These results  
584 highlight the PIROM's potential as a promising framework for optimizing multi-physical  
585 dynamical systems, such as TPS under diverse operating conditions.

## 586 A Technical Details

587 This appendix presents the technical details of the PIROM framework applied to the trans-  
 588ient modeling of thermo-ablative TPS. The first section provides the mathematical details  
 589 for the definition of the DG-FEM. The second section details the coarse-graining proce-  
 590 dures performed on the DG-FEM representation of the TPS. The third section presents the  
 591 derivation of the LCM model from an energy-conservation perspective.

### 592 A.1 Full-Order Model

593 To obtain the full-order numerical solution, the governing equation is spatially discretized  
 594 using variational principles of Discontinuous Galerkin (DG) to result in a high-dimensional  
 595 system of ordinary differential equations (ODEs). The DG-FEM model is written in an  
 596 element-wise form, which is beneficial for subsequent derivations of the lower-order models.  
 597 Note that the choice of DG approach here is mainly for theoretical convenience in the sub-  
 598 sequent coarse-graining formulation. In the numerical results, the full-order TPS ablation  
 599 simulations is computed using standard FEM instead, and the equivalence between DG and  
 600 standard FEM is noted upon their convergence.

#### 601 A.1.1 Domain Discretization

602 Consider a conforming mesh partition of the domain in Fig. 3, where each element belongs  
 603 to one and only one component. Denote the collection of all  $M$  elements as  $\{E_i\}_{i=1}^M$ . To ease  
 604 the description of the DG model, a graph structure is employed. The elements are treated  
 605 as vertices, the set of which is denoted  $\mathcal{V} = \{m\}_{m=1}^M$ . Two neighboring elements,  $E_i$  and  $E_j$ ,  
 606 are connected by an edge  $(i, j)$ , and the shared boundary between them is denoted  $e_{ij}$ . The  
 607 collection of all edges are denoted  $\mathcal{E}$ , and  $\mathcal{G}$  is referred to as a graph. In the graph, the edges  
 608 are unidirected, meaning if  $(i, j) \in \mathcal{E}$  then  $(j, i) \in \mathcal{E}$ . Furthermore, denote the neighbors  
 609 of the  $i$ -th element as  $\mathcal{N}_i = \{j | (i, j) \in \mathcal{E}\}$ . Lastly, for the ease of notation, introduce two  
 610 special indices:  $T$  for the boundary of an element that overlaps with the Dirichlet boundary  
 611 condition, and similarly  $q$  for the Neumann boundary condition.

#### 612 A.1.2 Weak Form of Discontinuous Galerkin Method

613 Choosing appropriate basis functions  $\phi_k$  and  $\phi_l$  and using the Interior Penalty Galerkin  
 614 (IPG) scheme [5], the variational bilinear form for eq. (1a) is,

$$\sum_{i=1}^M a_{\epsilon,i}(\phi_k, \phi_l) = \sum_{i=1}^M L_i(\phi_k) \quad (52)$$

615 where  $\epsilon$  is an user-specified parameter and,

$$a_{\epsilon,i}(\phi_k, \phi_l) = \int_{E^{(i)}} \left( \rho c_p \phi_k \frac{\partial \phi_l}{\partial t} + \nabla \phi_k \cdot (\mathbf{k} \nabla \phi_l) - \rho c_p \phi_k \mathbf{v} \cdot \nabla \phi_l \right) dE^{(i)} \quad (53a)$$

$$\begin{aligned} &= - \sum_{j \in \mathcal{N}_i \cup \{T_b\}} \int_{e_{ij}} \{ \mathbf{k} \nabla \phi_k \cdot n \} [\phi_l] de_{ij} + \epsilon \sum_{j \in \mathcal{N}_i \cup \{T_b\}} \int_{e_{ij}} \{ \mathbf{k} \nabla \phi_l \cdot n \} [\phi_k] de_{ij} \\ &\quad + \sigma \sum_{j \in \mathcal{N}_i \cup \{T_b\}} \int_{e_{ij}} [\phi_k] [\phi_l] de_{ij} \end{aligned} \quad (53b)$$

$$L_i(v) = \epsilon \sum_{j \in \mathcal{N}_i \cup \{T_b\}} \int_{e_{ij}} (\mathbf{k} \nabla \phi_l \cdot n) T_b de_{ij} + \int_{e_{iq}} \phi_k q_b de_{iq} + \sigma \int_{e_{iT}} \phi_k T_b de_{iT} \quad (53c)$$

616 In the bi-linear form above, the notations  $[]$  and  $\{ \}$  are respectively the jumps and averages  
617 at the boundary  $e_{ij}$  share by two elements  $E_i$  and  $E_j$ ,

$$[u] = u|_{E_i} - u|_{E_j}, \quad \{u\} = \frac{1}{2} \left( u|_{E_i} + u|_{E_j} \right), \quad \text{for } x \in e_{ij} = E_i \cap E_j$$

618 Furthermore, in the bi-linear form, the terms associated with  $\sigma$  are introduced to enforce  
619 the Dirichlet boundary conditions;  $\sigma$  is a penalty factor whose value can depend on the size  
620 of an element. Depending on the choice of  $\epsilon$ , the bi-linear form corresponds to symmetric  
621 IPG ( $\epsilon = -1$ ), non-symmetric IPG ( $\epsilon = 1$ ), and incomplete IPG ( $\epsilon = 0$ ). All these schemes  
622 are consistent with the original PDE and have similar convergence rate with respect to mesh  
623 size. In the following derivations, the case  $\epsilon = 0$  is chosen for the sake of simplicity.

### 624 A.1.3 Discontinuous Galerkin Model

625 Next, the DG-based model is written in an element-wise form. For the  $i$ -th element, use a  
626 set of  $P$  trial functions to represent the temperature as in eq. (6). Without loss of generality,  
627 the trial functions are assumed to be orthogonal, so that,

$$\int_{E_i} \phi_l^i(x) \phi_k^i(x) d\Omega = 0, \quad l \neq k$$

628 where  $|E_i|$  is the area ( $n_d = 2$ ) or volume ( $n_d = 3$ ) of the  $i$ -th element, and  $\delta_{lk}$  is the Kronecker  
629 delta function. Furthermore, for simplicity, choose  $\phi_1^i = 1$ . Thus, by orthogonality,

$$\int_{E_i} \phi_1^i(x) d\Omega = |E_i|, \quad \int_{E_i} \phi_k^i(x) d\Omega = 0, \quad k = 2, 3, \dots, P$$

630 Under the choice of basis functions,  $u_1^i$  is simply the average temperature of element  $E_i$ ,  
631 denoted as  $\bar{u}_i$ .

632 Using test functions same as trial functions, the dynamics  $\mathbf{u}^{(i)}$  is obtained by evaluating  
633 the element-wise bi-linear forms,

$$a_{\epsilon,i}(\phi_k^{(i)}, T^{(i)}) = L_i(\phi_k^{(i)}), \quad k = 1, 2, \dots, P \quad (54)$$

<sup>634</sup> Therefore, by standard variational principles, e.g., [5], the element-wise governing equation  
<sup>635</sup> is denoted as,

$$\mathbf{A}_i \dot{\mathbf{u}}_i = (\mathbf{B}_i + \mathbf{C}_i) \mathbf{u}_i + \sum_{j \in \mathcal{N}_i \cup \{T_b\}} (\mathbf{B}_{ij}^i \mathbf{u}_i + \mathbf{B}_{ij}^j \mathbf{u}_j) + \mathbf{f}_i(t), \quad \text{for } i = 1, 2, \dots, M \quad (55)$$

<sup>636</sup> where for  $k, l = 1, 2, \dots, P$ ,

$$[\mathbf{A}^{(i)}]_{kl} = \int_{E^{(i)}} \rho c_p \phi_k^{(i)} \phi_l^{(i)} dE^{(i)} \quad (56a)$$

$$[\mathbf{B}^{(i)}]_{kl} = - \int_{E^{(i)}} (\nabla \phi_k^{(i)}) \cdot (\mathbf{k} \nabla \phi_l^{(i)}) dE^{(i)} \quad (56b)$$

$$[\mathbf{C}^{(i)}]_{kl} = \int_{E^{(i)}} \rho c_p \phi_k^{(i)} \mathbf{v}^{(i)} \cdot \nabla \phi_l^{(i)} dE^{(i)} \quad (56c)$$

$$[\mathbf{B}_{ij}^{(i)}] = \int_{e_{ij}} \left\{ \mathbf{k} \nabla \phi_k^{(i)} \cdot \hat{n} \right\} \phi_l^{(i)} - \sigma [\phi_k^{(i)}] \phi_l^{(i)} de_{ij} \quad (56d)$$

$$[\mathbf{B}_{ij}^{(j)}] = \int_{e_{ij}} - \left\{ \mathbf{k} \nabla \phi_k^{(i)} \cdot \hat{n} \right\} \phi_l^{(j)} + \sigma [\phi_k^{(i)}] \phi_l^{(j)} de_{ij} \quad (56e)$$

$$[\mathbf{f}^{(i)}]_k = \int_{e_{iq}} \phi_k^{(i)} q_b de_{iq} + \sigma \int_{e_{iT}} \phi_k^{(i)} de_{iT} \quad (56f)$$

<sup>637</sup> The matrices  $\mathbf{A}^{(i)} \in \mathbb{R}^{P \times P}$ ,  $\mathbf{B}^{(i)} \in \mathbb{R}^{P \times P}$ , and  $\mathbf{C}^{(i)} \in \mathbb{R}^{P \times P}$  are respectively the capacitance,  
<sup>638</sup> conductivity, and advection matrices for element  $i$ . These matrices depend on  $\rho$ ,  $c_p$ ,  $\mathbf{k}$ , and  
<sup>639</sup>  $\mathbf{v}$ , and hence can be non-linear functions of  $\mathbf{u}^{(i)}$ . Since the trial functions are orthogonal, if  
<sup>640</sup>  $\rho c_p$  is constant within an element,  $\mathbf{A}^{(i)}$  is diagonal; otherwise,  $\mathbf{A}_i$  is symmetric and positive  
<sup>641</sup> definite as  $\rho c_p > 0$ .

<sup>642</sup> For compactness, the element-wise model in eq. (55) is also written in matrix form,

$$\mathbf{A} \dot{\mathbf{u}} = [\mathbf{B} + \mathbf{C}(\mathbf{u})] \mathbf{u} + \mathbf{f}(t) \quad (57)$$

<sup>643</sup> where  $\mathbf{u} = [\mathbf{u}^{(1)}, \mathbf{u}^{(2)}, \dots, \mathbf{u}^{(M)}]^T \in \mathbb{R}^{MP}$  includes all DG variables,  $\mathbf{f} = [\mathbf{f}^{(1)}, \mathbf{f}^{(2)}, \dots, \mathbf{f}^{(M)}]^T \in \mathbb{R}^{MP}$ ,  $\mathbf{A}$  and  $\mathbf{C}$  are matrices of  $M$  diagonal blocks whose  $i$ -th blocks are  $\mathbf{A}^{(i)}$  and  $\mathbf{C}^{(i)}$ , and  
<sup>644</sup>  $\mathbf{B}$  is a matrix of  $M \times M$  blocks whose  $(i, j)$ -th block is,

$$\mathbf{B}_{ij} = \begin{cases} \mathbf{B}^{(i)} + \sum_{j \in \mathcal{N}_i \cup \{T_b\}} \mathbf{B}_{ij}^{(i)}, & i = j \\ \mathbf{B}_{ij}^{(j)}, & i \neq j \end{cases} \quad (58)$$

<sup>646</sup> The dependency of  $\mathbf{C}$  on  $\mathbf{u}$  is explicitly noted in eq. (57), which is the main source of non-  
<sup>647</sup> linearity in the current TPS problem. Moreover, the mesh velocity  $\mathbf{v}$  varies with space  
<sup>648</sup> and time, and thus the advection matrix  $\mathbf{C}$  varies with time as a function of the surface  
<sup>649</sup> temperature  $T_q(x, t)$ .

## 650 A.2 Coarse-Graining of Dynamics

651 The LCM is obtained by coarse-graining the full-order DG-FEM. This coarse-graining procedure produces resolved  $\mathbf{r}^{(1)}(\mathbf{u}, t)$  and residual  $\mathbf{r}^{(2)}(\mathbf{u}, t)$  dynamics as in eq. (24). This section  
652 presents the detail derivations and magnitude analysis for the resolved and residual dynamics.  
653

### 655 A.2.1 Resolved Dynamics

656 Using eq. (21), the resolved dynamics is computed as follows,

$$\mathbf{r}^{(1)}(\mathbf{u}, t) = \mathcal{P} [\Phi^+ \mathbf{A}(\mathbf{u})^{-1} (\mathbf{B}(\mathbf{u})\mathbf{u} + \mathbf{C}(\mathbf{u})\mathbf{u} + \mathbf{f}(t))] \quad (59a)$$

$$\begin{aligned} &= \Phi^+ \mathbf{A}(\mathbf{Pu})^{-1} \mathbf{PB}(\mathbf{Pu}) \mathbf{Pu} + \Phi^+ \mathbf{A}(\mathbf{Pu})^{-1} \mathbf{PC}(\mathbf{Pu}) \mathbf{Pu} \\ &\quad + \Phi^+ \mathbf{A}(\mathbf{Pu})^{-1} \mathbf{Pf}(t, \mathbf{Pu}) \end{aligned} \quad (59b)$$

$$\begin{aligned} &= \underbrace{\Phi^+ \mathbf{A}(\Phi \bar{\mathbf{u}})^{-1} \Phi}_{\#1} \underbrace{\Phi^+ \mathbf{B}(\Phi \bar{\mathbf{u}}) \Phi \bar{\mathbf{u}}}_{\#2} + \Phi^+ \mathbf{A}(\Phi \bar{\mathbf{u}})^{-1} \underbrace{\Phi \Phi^+ \mathbf{C}(\Phi \bar{\mathbf{u}}) \Phi \bar{\mathbf{u}}}_{\#3} \\ &\quad + \Phi^+ \mathbf{A}(\Phi \bar{\mathbf{u}})^{-1} \underbrace{\Phi \Phi^+ \mathbf{f}(t, \Phi \bar{\mathbf{u}})}_{\#4} \end{aligned} \quad (59c)$$

657 Detailed derivations for the #1, #2, and #4 terms can be found in Ref. [17]. The effects of  
658 coarse-graining on the advection term #3 are analyzed next.

659 **Term #3** The  $\mathbf{C}(\mathbf{u}) \in \mathbb{R}^{MP \times MP}$  matrix contains  $M$  diagonal of size  $P \times P$ , since the  
660 basis functions are defined locally on each element. Therefore,  $[\mathbf{C}(\mathbf{u})]_{ij} = \mathbf{0}$  for all  $i \neq j$  with  
661  $i, j = 1, 2, \dots, M$ . It follows that for  $k, l = 1, 2, \dots, N$ ,

$$[\Phi^+ \mathbf{C}(t, \Phi \bar{\mathbf{u}}) \Phi]_{kl} = \sum_{i=1}^M \sum_{j=1}^M \boldsymbol{\varphi}_i^{k+} [\mathbf{C}(t, \Phi \bar{\mathbf{u}})]_{ij} \boldsymbol{\varphi}_j^l \quad (60a)$$

$$= \sum_{i=1}^M \boldsymbol{\varphi}_i^{k+} [\mathbf{C}(t, \Phi \bar{\mathbf{u}})]_{ii} \boldsymbol{\varphi}_i^l \quad (60b)$$

$$= \sum_{i \in \mathcal{V}_k} \boldsymbol{\varphi}_i^{k+} [\mathbf{C}(t, \Phi \bar{\mathbf{u}})]_{ii} \boldsymbol{\varphi}_i^l \quad (60c)$$

662 where in the second row, the fact that  $[\mathbf{C}(\mathbf{u})]_{ij} = 0$  for all  $i \neq j$  is used, and in the last row,  
663 the fact that  $\boldsymbol{\varphi}_i^{k+} = 0$  for all  $i \notin \mathcal{V}_k$  is used. Now, considering that  $[\mathbf{C}(\mathbf{u})]_{ii}$  has a (1, 1)-th  
664 zero element, i.e.,  $[\mathbf{C}_{11}(t, \Phi \bar{\mathbf{u}})]_{ii} = 0$ , and that if  $k \neq l$  then  $i \notin \mathcal{V}_l$  and thus  $\boldsymbol{\varphi}_i^l = \mathbf{0}$ , it follows  
665 that for some index  $i \in \mathcal{V}_k$ ,

$$\boldsymbol{\varphi}_i^{k+} [\mathbf{C}(t, \Phi \bar{\mathbf{u}})]_{ii} \boldsymbol{\varphi}_i^l = \boldsymbol{\varphi}_i^{k+} [\mathbf{C}(t, \Phi \bar{\mathbf{u}})]_{ii} \boldsymbol{\varphi}_i^k = \frac{|E_i|}{|\Omega_k|} [\mathbf{C}_{11}(t, \Phi \bar{\mathbf{u}})]_{ii} = 0 \quad (61)$$

666 The matrix  $[\Phi^+ \mathbf{C}(t, \Phi \bar{\mathbf{u}}) \Phi]_{kl} = 0$  for all  $k, l = 1, 2, \dots, N$ , and thus,

$$\bar{\mathbf{C}}(t, \bar{\mathbf{u}}) = \Phi^+ \mathbf{C}(t, \Phi \bar{\mathbf{u}}) \Phi = \mathbf{0} \quad (62)$$

667 as indicated by the LCM in eq. (11).

### 668 A.2.2 Magnitude Analysis for Residual Dynamics

669 Next, the magnitude of the residual dynamics  $\mathbf{r}^{(2)}(\mathbf{u}, t)$  is analyzed to pinpoint the missing  
670 physics in the LCM. By definition,

$$\mathbf{r}^{(2)}(\mathbf{u}, t) = \dot{\bar{\mathbf{u}}} - \mathbf{r}^{(1)}(\bar{\mathbf{u}}, t) \quad (63a)$$

$$= \Phi^+ \mathbf{r}(\mathbf{u}, t) - \mathbf{r}^{(1)}(\mathbf{u}, t) \quad (63b)$$

$$\begin{aligned} &= \underbrace{\Phi^+ \mathbf{A}(\mathbf{u})^{-1} \mathbf{B}(\mathbf{u}) \mathbf{u} - \bar{\mathbf{A}}(\bar{\mathbf{u}})^{-1} \bar{\mathbf{B}}(\bar{\mathbf{u}}) \bar{\mathbf{u}}}_{\#1} + \underbrace{\Phi^+ \mathbf{A}(\mathbf{u})^{-1} \mathbf{C}(\mathbf{u}) \mathbf{u} - \bar{\mathbf{A}}(\bar{\mathbf{u}})^{-1} \bar{\mathbf{C}}(t, \bar{\mathbf{u}}) \bar{\mathbf{u}}}_{\#2} \\ &\quad + \underbrace{\Phi^+ \mathbf{A}(\mathbf{u})^{-1} \mathbf{f}(t) - \bar{\mathbf{A}}(\bar{\mathbf{u}})^{-1} \bar{\mathbf{f}}(t)}_{\#3} \end{aligned} \quad (63c)$$

671 The magnitude analysis for terms  $\#1$  and  $\#3$  can be found in Ref. [17]. The analysis for  
672 term  $\#2$  is presented next. Let  $\mathbf{D}(\bar{\mathbf{u}}) = \mathbf{A}(\Phi \bar{\mathbf{u}})^{-1} \mathbf{P} \mathbf{C}(t, \Phi \bar{\mathbf{u}})$ , then,

$$\Phi^+ \mathbf{A}(\mathbf{u})^{-1} \mathbf{C}(\mathbf{u}) \mathbf{u} - \bar{\mathbf{A}}(\bar{\mathbf{u}})^{-1} \bar{\mathbf{C}}(t, \bar{\mathbf{u}}) \bar{\mathbf{u}} \quad (64a)$$

$$= \Phi^+ \mathbf{A}(\mathbf{u})^{-1} \mathbf{C}(\mathbf{u}) \mathbf{u} - \Phi^+ \mathbf{A}(\Phi \bar{\mathbf{u}})^{-1} \mathbf{P} \mathbf{C}(t, \Phi \bar{\mathbf{u}}) \Phi \Phi^+ \mathbf{u} \quad (64b)$$

$$= \Phi^+ \mathbf{A}^{-1}(\mathbf{u}) \mathbf{C}(\mathbf{u}) \mathbf{u} - \Phi^+ \mathbf{D}(\bar{\mathbf{u}}) \Phi \Phi^+ \mathbf{u} \quad (64c)$$

$$(64d)$$

673 where  $\mathbf{P} = \Phi \Phi^+$ . Thus,

$$\|\Phi^+ \mathbf{A}(\mathbf{u})^{-1} \mathbf{C}(\mathbf{u}) \mathbf{u} - \bar{\mathbf{A}}(\bar{\mathbf{u}})^{-1} \bar{\mathbf{C}}(t, \bar{\mathbf{u}}) \bar{\mathbf{u}}\| \quad (65a)$$

$$\leq \|\Phi^+ \mathbf{A}^{-1}(\mathbf{u}) \mathbf{C}(\mathbf{u}) \mathbf{u} - \Phi^+ \mathbf{D}(\bar{\mathbf{u}}) \mathbf{u}\| + \|\Phi^+ \mathbf{D}(\bar{\mathbf{u}}) \mathbf{u} - \Phi^+ \mathbf{D}(\bar{\mathbf{u}}) \Phi \Phi^+ \mathbf{u}\| \quad (65b)$$

$$\leq \|\Phi^+ \| \underbrace{\|\mathbf{A}^{-1}(\mathbf{u}) \mathbf{C}(\mathbf{u}) \mathbf{u} - \mathbf{D}(\bar{\mathbf{u}}) \mathbf{u}\|}_{\#1} + \|\Phi^+ \mathbf{D}(\bar{\mathbf{u}})\| \underbrace{\|\mathbf{u} - \Phi \Phi^+ \mathbf{u}\|}_{\#2} \quad (65c)$$

674 where term  $\#2$  is due to the approximation of non-uniform temperature as constants, and  
675 term  $\#1$  is the error in the advection dynamics due to coarse-graining.

### 676 A.3 Lumped Capacitance Model

677 The following assumptions are employed: (1) the temperature in component  $(i)$  is described  
678 by a scalar time-varying average temperature  $\bar{u}^{(i)}$ , (2) between neighboring components  $(i)$

679 and (j) the heat flux is approximated as,

$$q_{ij} = \frac{\bar{u}^{(j)} - \bar{u}^{(i)}}{R_{ij}} \quad (66)$$

680 where  $R_{ij}$  is the thermal resistance. Empirically, for a component of isotropic heat conduction  
681 conductivity  $k$ , length  $\ell$ , and cross-section area  $A$ , the thermal resistance is  $R = \ell/kA$ . Between  
682 components  $i$  and  $j$ , define  $R_{ij} = R_i + R_j$ . In addition, the heat flux due to Dirichlet  
683 boundary condition is computed as  $q_{iT} = (T_b - \bar{u}^{(i)})/R_i$ .

684 At component  $i$ , the dynamics of LCM are given by,

$$\int_{E^{(i)}} \rho c_p \dot{\bar{u}}^{(i)} dE^{(i)} = \left( \sum_{j \in \mathcal{N}_i} \int_{e_{ij}} \frac{\bar{u}^{(j)} - \bar{u}^{(i)}}{R_{ij}} de_{ij} \right) + \int_{e_{iq}} q_b de_{iq} + \int_{e_{iT}} \frac{T_b - \bar{u}^{(i)}}{R_i} de_{iT} \quad (67a)$$

$$\bar{A}^{(i)} \dot{\bar{u}}^{(i)} = \left( \sum_{j \in \mathcal{N}_i} \frac{|e_{ij}|}{R_{ij}} (\bar{u}^{(j)} - \bar{u}^{(i)}) \right) + |e_{iq}| \bar{q}^{(i)} + \frac{|e_{iT}|}{R_i} (\bar{T}^{(i)} - \bar{u}^{(i)}) \quad (67b)$$

$$= \sum_{j \in \mathcal{N}_i} \left( -\frac{|e_{ij}|}{R_{ij}} \bar{u}^{(i)} + \frac{|e_{ij}|}{R_{ij}} \bar{u}^{(j)} \right) + \left( -\frac{|e_{iT}|}{R_i} \bar{u}^{(i)} \right) + \left( |e_{iq}| \bar{q}^{(i)} + \frac{|e_{iT}|}{R_i} \bar{T}^{(i)} \right) \quad (67c)$$

$$= \sum_{j \in \mathcal{N}_i \cup \{T_b\}} \left( \bar{B}_{ij}^{(i)} \bar{u}^{(i)} + \bar{B}_{ij}^{(j)} \bar{u}^{(j)} \right) + \bar{f}^{(i)} \quad (67d)$$

685 where in eq. (67b)  $|e|$  denotes the length ( $d = 2$ ) or area ( $d = 3$ ) of a component boundary  
686  $e$ . The  $\bar{A}^{(i)}$ ,  $\bar{B}_{ij}^{(i)}$ , and  $\bar{B}_{ij}^{(j)}$  quantities are provided in eq. (14).

687 The lumped-mass representation for the four-component TPS is shown in Fig. ???. Let  
688  $v_i$  represent the area of the  $i$ -th element,  $\overline{\rho c_{p,i}}$ , the heat capacity evaluated using the average  
689 temperature  $\bar{u}^{(i)}$ , and  $1/R_{ij} = 1/R_i(\bar{u}^{(i)}) + 1/R_j(\bar{u}^{(j)})$  the equivalent thermal resistance  
690 between elements  $i$  and  $j$ . Leveraging the formulas from eqs. (13) and (14), the LCM  
691 matrices are given by,

$$\bar{\mathbf{A}} = \begin{bmatrix} \overline{\rho c_{p,1}} v_1 & 0 & 0 & 0 \\ 0 & \overline{\rho c_{p,2}} v_2 & 0 & 0 \\ 0 & 0 & \overline{\rho c_{p,3}} v_3 & 0 \\ 0 & 0 & 0 & \overline{\rho c_{p,4}} v_4 \end{bmatrix}, \quad (68a)$$

$$\bar{\mathbf{B}} = \begin{bmatrix} \frac{1}{R_{12}} + \frac{1}{R_{14}} & -\frac{1}{R_{12}} & 0 & -\frac{1}{R_{14}} \\ -\frac{1}{R_{12}} & \frac{1}{R_{12}} + \frac{1}{R_{24}} + \frac{1}{R_{23}} & -\frac{1}{R_{23}} & -\frac{1}{R_{24}} \\ 0 & -\frac{1}{R_{32}} & \frac{1}{R_{32}} + \frac{1}{R_{34}} & -\frac{1}{R_{34}} \\ -\frac{1}{R_{14}} & -\frac{1}{R_{24}} & -\frac{1}{R_{34}} & \frac{1}{R_{14}} + \frac{1}{R_{24}} + \frac{1}{R_{34}} \end{bmatrix}, \quad \bar{\mathbf{f}} = \begin{bmatrix} \bar{q}^{(1)} \\ \bar{q}^{(2)} \\ \bar{q}^{(3)} \\ 0 \end{bmatrix} \quad (68b)$$

## 692 References

- 693 [1] Adam J. Amar, A. Brandon Oliver, Benjamin S. Kirk, Giovanni Salazar, and Justin  
694 Droba. Overview of the charring ablator response (char) code. In AIAA, editor, *AIAA*

- 695        *Aviation Forum*, 2016.
- 696 [2] Guy L. Bergel, Frank B. Beckwith, Gabel J. de Frias, Kevin M. Manktelow, Mark T.  
 697        Merewether, Scott T. Miller, Krishen J. Parmar, Timothy S. Shelton, Jesse T. Thomas,  
 698        Jeremy T. Trageser, Benjamin T. Treweek, Michael V. Veilleux, and Ellen B. Wagman.  
 699        *Sierra/SolidMechanics 5.6 User's Manual*, 2022.
- 700 [3] Ricky T. Q. Chen, Yulia Rubanova, Jesse Bettencourt, and David Duvenaud. Neural  
 701        ordinary differential equations, 2019.
- 702 [4] Jonathan Clausen, Victor Brunini, Lincoln Collins, Robert C Knaus, Alec Kucala,  
 703        Stephen Lin, Daniel Robert Moser, Malachi Phillips, Thomas Michael Ransegrenola,  
 704        Samuel Ramirez Subia, et al. Sierra multimechanics module: Aria verification manual-  
 705        version 5.22. Technical report, Sandia National Lab.(SNL-NM), Albuquerque, NM  
 706        (United States), 2024.
- 707 [5] Gary Cohen and Sebastien Pernet. *Finite Element and Discontinuous Galerkin Methods*  
 708        for Transient Wave Equations. Springer Dordrecht, Le Chesnay and Toulouse France,  
 709        2018.
- 710 [6] Jianhao Fang, Weifei Hu, Zhenyu Liu, Yuhao Zhou, Chao Wei, and Jianrong Tan. A  
 711        reduced order finite element-informed surrogate model for approximating global high-  
 712        fidelity simulations. *Structural and Multidisciplinary Optimization*, 67(12), 2024.
- 713 [7] Matthew Gasch, Keith Peterson, Mairead Stackpoole, Ethiraj Venkatapathy, Gregory  
 714        Gonzales, and Kyle Hendrickson. Development of advanced ablative carbon phenolic  
 715        tps for future nasa missions and commercial space. In *38th Annual Small Satellite*  
 716        *Conference*, Logan, Utah, May 2024.
- 717 [8] Micah A. Howard and Ben F. Blackwell. A multi-dimensional finite element based solver  
 718        for decomposing and non-decomposing thermal protection systems. In AIAA, editor,  
 719        *AIAA Aviation Forum*, 2015.
- 720 [9] Frank P. Incropera, David P. DeWitt, Theodore L. Bergman, and Adrienne S. Lavine.  
 721        *Fundamentals of Heat and Mass Transfer*. Wiley, Hoboken, NJ, 7th edition, 2011.
- 722 [10] R. J. Klock and Carlos Cesnik. Nonlinear thermal reduced-order modeling for hypersonic  
 723        vehicles. *AIAA Journal*, 55(7), 2017.
- 724 [11] Arun Govind Neelan. Linear and non-linear reduced order model of scramjet. In *Advances*  
 725        *in Multidisciplinary Design, Analysis and Optimization*, pages 111–118, Singapore,  
 726        2025.
- 727 [12] Alberto Padovan, Blaine Vollmer, Francesco Panerai, Marco Panesi, Kelly A. Stephani,  
 728        and Daniel J. Bodony. An extended bformulation for ablating-surface boundary condi-  
 729        tions. *International Journal of Heat and Mass Transfer*, 218:124770, 2024.
- 730 [13] Eric Parish and Karthik Duraisamy. Non-markovian closure models for large eddy  
 731        simulations using the mori-zwanzig formalism. *Phys. Rev. Fluids*, 2:014604, Jan 2017.

- 732 [14] Eric Parish and Karthik Duraisamy. A unified framework for multiscale modeling using  
733 the mori-zwanzig formalism and the variational multiscale method. *ArXiv*, 12 2017.
- 734 [15] Eric Parish and Karthik Duraisamy. *Coarse-Graining Turbulence Using the*  
735 *Mori-Zwanzig Formalism*. Cambridge University Press, Cambridge, 2025.
- 736 [16] Adam Thelen, Xiaoge Zhang, Olga Fink, Yan Lu, Sayan Ghosh, Byeng D. Youn,  
737 Michael D. Todd, Sankaran Mahadean, Chao Hu, and Zhen Hu. A comprehensive  
738 review of digital twin – part 1: modeling and twinning enabling technologies. *Structural*  
739 *and Multidisciplinary Optimization*, 65(12), 2022.
- 740 [17] Carlos A. Vargas Venegas, Daning Huang, Patrick Blonigan, and JohnTencer. Physics-  
741 infused reduced-order modeling for analysis of multi-layered hypersonic thermal protec-  
742 tion systems, 2025.
- 743 [18] Yongyong Xian, Baisong Pan, and Luping Luo. A new model updating strategy with  
744 physics-based and data-driven models. *Structural and Multidisciplinary Optimization*,  
745 64(1), 2021.
- 746 [19] Yin Yu, John Harlim, Daning Huang, and Yan Li. Learning coarse-grained dynamics  
747 on graph. *arXiv preprint arXiv:2405.09324*, 2024.